

FINAL REPORT

Taiwan – USA AFOSR Nanoscience Initiative

(AOARD-074079)

**Single-molecule luminescence and high efficiency
photovoltaic cells based on percolated conducting
carbon nanotubes scaffolds templated with
light-harvesting conjugated polymers and
nanohybrids**

Principal Investigator

Arnold C.-M. Yang

acyang@mse.nthu.edu.tw

Department of Materials Science and Engineering

National Tsing Hua University

101, Kuang Fu Road, Section 2, Hsinchu City, Taiwan

Phone: +886-3-572-0792, FAX: +886-3-572-2366

Report Documentation Page

Form Approved
OMB No. 0704-0188

Public reporting burden for the collection of information is estimated to average 1 hour per response, including the time for reviewing instructions, searching existing data sources, gathering and maintaining the data needed, and completing and reviewing the collection of information. Send comments regarding this burden estimate or any other aspect of this collection of information, including suggestions for reducing this burden, to Washington Headquarters Services, Directorate for Information Operations and Reports, 1215 Jefferson Davis Highway, Suite 1204, Arlington VA 22202-4302. Respondents should be aware that notwithstanding any other provision of law, no person shall be subject to a penalty for failing to comply with a collection of information if it does not display a currently valid OMB control number.

1. REPORT DATE 14 JAN 2009	2. REPORT TYPE	3. DATES COVERED		
4. TITLE AND SUBTITLE Single-molecule Luminescence and High Efficiency Photovoltaic Cells Based on Conducting Crosslinked Carbon Nanotube Scaffolds Templated with Light-Harvesting Conjugated Polymers and Nanohybrids		5a. CONTRACT NUMBER FA48690714079		
		5b. GRANT NUMBER		
		5c. PROGRAM ELEMENT NUMBER		
6. AUTHOR(S) Arnold Chang-Mou Yang		5d. PROJECT NUMBER		
		5e. TASK NUMBER		
		5f. WORK UNIT NUMBER		
7. PERFORMING ORGANIZATION NAME(S) AND ADDRESS(ES) National Tsing Hua University, 101, Kuang Fu Rd, Sec 2, Hsinchu, Taiwan, NA, 30043		8. PERFORMING ORGANIZATION REPORT NUMBER N/A		
9. SPONSORING/MONITORING AGENCY NAME(S) AND ADDRESS(ES)		10. SPONSOR/MONITOR'S ACRONYM(S)		
		11. SPONSOR/MONITOR'S REPORT NUMBER(S)		
12. DISTRIBUTION/AVAILABILITY STATEMENT Approved for public release; distribution unlimited.				
13. SUPPLEMENTARY NOTES				
14. ABSTRACT This project describes the successful preparation of the novel photoelectric material poly(2-methoxy-5-(2-ethylhexyloxy)-1,4-phenylenevinylene)-grafted multiwall carbon nanotubes and some of this material's photoelectric properties.				
15. SUBJECT TERMS				
16. SECURITY CLASSIFICATION OF:			17. LIMITATION OF ABSTRACT	
a. REPORT unclassified	b. ABSTRACT unclassified	c. THIS PAGE unclassified		
			18. NUMBER OF PAGES 68	19a. NAME OF RESPONSIBLE PERSON

Abstract

In this research, nanocomposites constructed by surface-grafted multiwalled carbon nanotubes (CNTs) with conjugated polymers dispersed in a polymer matrix were synthesized to form novel optoelectronic materials that exploit single-molecule effects. During the course of the execution of the proposal, research work was focused on three parts: 1. the synthesis work of the nanocomposite of light-harvesting polymers on percolated carbon nanotubes, 2. single-molecule luminescence of conjugated polymers as affected by chain confinement effect, and 3. the nano-scale mechanical interactions between the CNTs and the polymer chain in the matrix. These three parts are interlinked in that the grafted polymer layer on CNTs are in fact molecularly confined macromolecules due to the strong π - π interactions with the graphene surfaces and the small thickness that imposes large molecular deformation of the anchored chains. Furthermore, nanoscale interactions between the polymer chains and CNTs are very help to reveal the actual packing and dynamic relationship in the nanocomposites. It is also later unveiled that the mechanical characteristics of polymer chains in the sub-molecular level may strongly influence the optoelectronic behavior of the conjugated polymers.

At the end of the work, we have successfully prepared the novel photoelectric material, poly (2-methoxy-5-(2'-ethylhexyloxy)-1, 4-phenylene vinylene)-grafted MWCNTs ((MEH-PPV)-grafted MWCNTs), was synthesized via a surface grafting method. The (MEH-PPV)-grafted MWCNTs exhibited photo-excited phenomenon and generated significant photocurrents upon illumination. Very large photocurrents as compared to the neat polymer (by 375 times) were observed. The effects the molecular weight of the grafted polymer were investigated. A Schottky model was used to interpret the observed effect due to variation of the band gap of MEH-PPV and photo-induced electron transfer (PET), indicating that appropriate band gap of the grafting MEH-PPV results in PET more efficiently. The effect of coating thickness of MEH-PPV was revealed that thicker MEH-PPV enhances larger photocurrents and decreases the occurrence of short circuit. An organic photovoltaic cell, where the (MEH-PPV)-grafted MWCNTs (MWCNT content = 34 wt.-%) was used as the photoactive layer, was also investigated to prove that coating MEH-PPV contributes to inhibit short circuit. The current work represents the first successful nanocomposites based on covalently grafted CNT with conjugated polymers that shows outstanding optoelectronic performance. More work in this research direction is still undergoing in our lab to unveil further details and new properties of the nanocomposites.

For the second part of the work, by exploring the nanoplastic flows (crazing or shear yielding) of diluted blends of the light-harvesting polymer (MEH-PPV) in an optically inert polymer matrix (polystyrene), we have discovered the extraordinarily large optoelectronic quantum efficiency of conjugated polymer arising from extreme stretching (~ 300% strain). This enhancement can go up to around 150 times, as compared to the unstretched, but only occur in the cases of single-molecule luminescence where each light-harvesting macromolecule is separated from each other. Self-trapping of the photo-induced charges was used to explain this new observation. In the highly stretched polymer chains, self-trapping had become difficult to occur due to the dramatically increase of local deformation energy of the stretch-hardened chains. Further exploration is still undergoing while a paper is been written up for submission.

The chain confinement effect was also found occurring in the ultrathin films system of the conjugated polymer where the luminescence efficiency was also found to increase more than 150 times for ~2 nm thick monolayer films. The monolayer was resulted from thermal dewetting of films with thickness in the range from 10 to 60 nm. No significant shift of the spectrum was observed as a result of the chain confinement. A paper is being written for submission. Further to this work, solvent annealing was found to replicate the thermal annealing effect where ultrathin monolayer polymer films were produced to show this remarkable phenomenon. The discovery of this alternative way to achieve the large efficiency gain paves a new route for feasible applications exploiting this large chain confinement effect. Continuous work is also undergoing.

For the third part of the work, surface-grafted multiwalled CNTs dispersed in two model polymer systems, polystyrene (PS) and poly(phenylene oxide) (PPO), representing respectively brittle and ductile polymers. Although significant mechanical reinforcement in the both systems was observed, drastically different microscopic interactions, engendered from variations in the fundamental behavior of entangled chains, were noted during the nanoplastic flow of crazing or shear yielding in the nanocomposites. As revealed by a local stress analysis based on atomic force microscopy, “extensibility” of the entanglement network determines not only the mode of deformation leading to either crazing or shear yielding but also how the stretched chains interact with individual nanotubes. The results bear important implications on our understanding toward the fundamental behavior of entangled macromolecules in the glassy state.

Chapter I

Light-harvesting Polymers on Percolated Carbon Nanotubes

Since their discovery [1], carbon nanotubes (CNTs) have attracted considerable attentions due to remarkable thermal, electronic and mechanical properties [2-6]. Particularly, CNTs are promising electronic materials to provide higher exciton dissociation volume and increase mobility for carrier transport for organic photovoltaic devices due to their excellent electrical conductivity [7-9], great aspect ratios and photo-induced electron transfer (PET) [10, 11]. Several researches [12, 21, 22] have demonstrated that incorporation of CNTs in a polymeric host increases the electrical conductivity of CNT/polymer nanocomposites, indicating that CNTs provide unimpeded paths for electron transport after the percolation threshold. PET is an electron transfer [13], which is observed when ordinary fluorescence emission is quenched by the presence of an electron acceptor embedded in the conjugated polymer and the conjugated polymer (electron donor) transfers electrons to the electron acceptor in its excited state. MWCNTs are also known to quench emission efficiently from conjugated polymers [14,15] due to PET. Thus, CNTs is a good candidate to provide more interfaces for exciton dissociation and increase carrier mobility for organic photovoltaic devices. Hence, CNTs are used to incorporate with conjugated polymers in organic solar cells (OSCs) [16-19]. In this polymer/CNT nanocomposite, excitons were generated on conjugated polymers under illumination and were dissociated at the interfaces of polymer/CNT due to charge transfer, where electrons were transported by CNTs and holes were transported through conjugated polymers. Although CNTs possess many advantages for applications in OSCs, CNTs would tend to result in short circuit because of their contact. In order to investigate optoelectronic properties of CNT/conjugated polymer nanocomposites, a novel material, poly (2-methoxy-5-(2'-ethylhexyloxy)-1, 4-phenylene vinylene)-grafted MWCNTs ((MEH-PPV)-grafted MWCNTs), was synthesized by means of a surface grafting method. Furthermore, the grafting MEH-PPV coating on MWCNT surface was expected to contribute to inhibit short circuit.

I-1 Experimental Procedures:

I-1.1 Synthesis of MEH-PPV-grafted MWCNTs

MEH-PPV monomers were produced by alkylating and then chloromethylating 4-methoxyphenol. At first, 4-methoxyphenol, 2-ethylhexyl bromide, potassium hydroxide (KOH), tetrabutylammonium bromide as a surfactant and deionized water as the solvent were added to form 1-(2-ethylhexyloxy)-4-methoxybenzene under nitrogen inlet at 100 °C for 3 days. Then, by adding 1-(2-ethylhexyloxy)-4-methoxybenzene, para-formaldehyde, hydrobromic acid (HBr)

and glacial acetic acid as the solvent under nitrogen inlet at 70 °C for 4 h (Figure 1) to form 1-(2-ethylhexyloxy)-2,5-bis(bromomethyl)-4-methoxybenzene (MEH-PPV monomer).

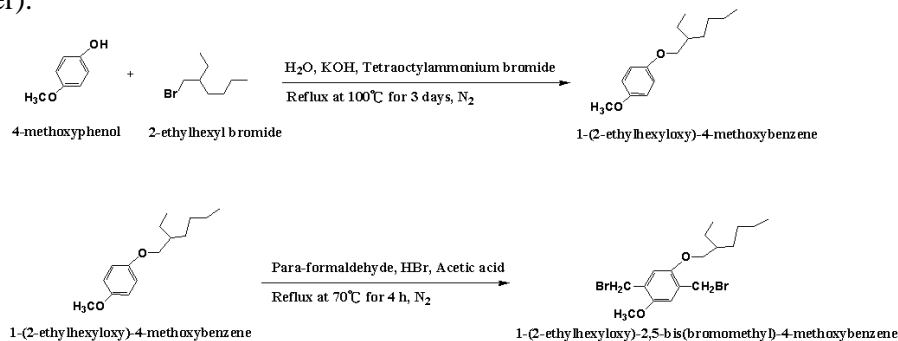


Figure 1. Synthesis procedure of MEH-PPV monomers: the side chain was grafted to 4-methoxyphenol and then $-\text{CH}_2\text{Br}$ groups were grafted to 1-(2-ethylhexyloxy)-4-methoxybenzene.

MWCNTs synthesized via a chemical vapor deposition method (purchased from DESUN Nano Inc., Taiwan) had tube diameter of 10–30 nm and 5–15 μm in length. The as-received sample of MWCNTs were treated in a mixture of concentrated H_2SO_4 (98 wt %) and concentrated HNO_3 (16 M) (v/v=3/2) at 150 °C for 1.5 h, resulting in attachment of carboxyl groups ($-\text{COOH}$) on the MWCNT surface. The acid-treated MWCNTs were added with MEH-PPV monomers and pyridine to attach the monomers on the MWCNT surface with ultrasonication in THF. Then, (MEH-PPV monomer)-grafted MWCNTs and MEH-PPV monomers were mixed homogeneously in THF to grow MEH-PPV chains on MWCNT surface via adding potassium tert-butoxide (tBuOK) under dark condition and nitrogen inlet at 5 °C as shown in Figure 2. By tuning different stoichiometry of tBuOK and reaction time, molecular weight and weight contents of the grafting MEH-PPV could be tuned.

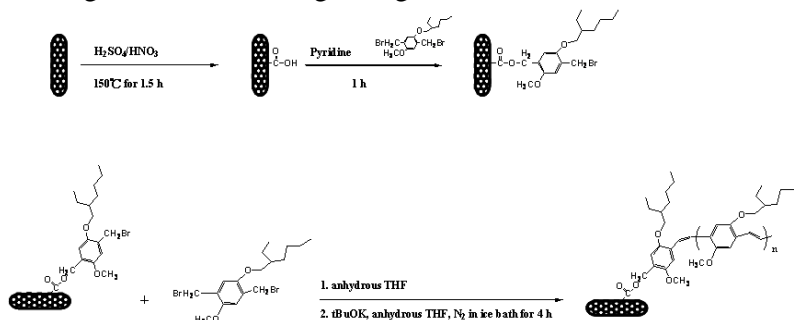


Figure 2. Synthesis procedure of MEH-PPV-grafted MWCNTs: the formation of MWCNT-g-(MEH-PPV monomer) and the growth of MEH-PPV chains from MWCNTs.

I-1.2 Device Fabrication of the Organic Photovoltaic Cell

The photovoltaic cell was fabricated on patterned indium tin oxide (ITO) coated on glass substrates with a sheet resistance of 13 ± 2 ohm/square and the thickness of 125 nm. The ITO/glass substrate was washed by a detergent and then cleaned with ultrasonication in deionized water, acetone and then isopropanol for 10 minutes respectively. In order to hole transport and modification of ITO surface, PEDOT was coated on the ITO substrate by spin coating to form a 40 nm thin film. Then, the photoactive layer, (MEH-PPV)-grafted MWCNTs, was coated by dropping with the thickness of 10 μm . Finally, the layers of TPBi (32 nm), LiF (0.7 nm) and Al (150 nm), were deposited by a CVD (Figure 3).

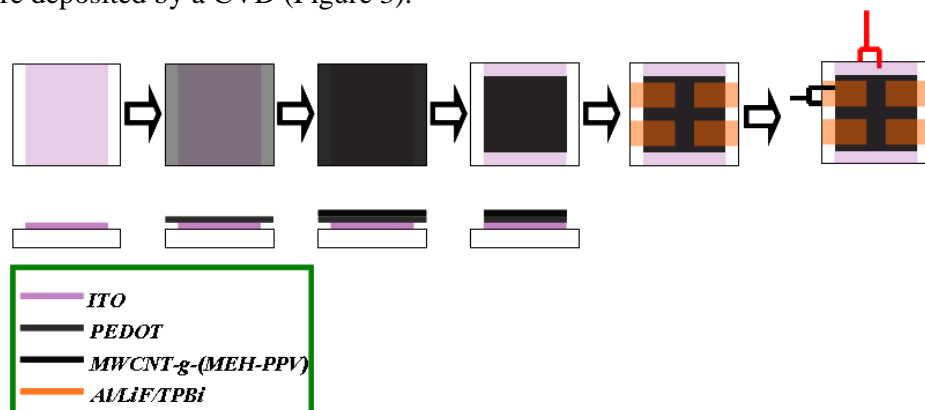


Figure 3. Device fabrication of the organic photovoltaic cell where (MEH-PPV)-grafted MWCNTs was served as the photoactive layer.

I-1.3 Characterizations

Fourier-Transform Infrared spectroscopy (FT-IR) was used to monitor the functional groups of the grafting polymer with an infrared spectrophotometer (Bomem DA8.3) recording between 4000 and 400 cm^{-1} . TGA was performed under Ar atmosphere with a heating rate of 10 $^{\circ}\text{C}/\text{min}$ (Perkin-Elmer thermal analysis TG/DTA system). The microstructures of the samples were examined under a TEM of JOEL JEM-2010 with acceleration voltage of 200 KeV. Measurements of molecular weight and polydispersity index (PDI) of the grafting MEH-PPV chains (after being cleaved from MWCNTs by KOH refluxing) were carried out by using GPC analyses with PS standard calibrations. Band gap of MEH-PPV was determined by UV-visible spectrum (Hitachi U-3010 UV- visible spectrophotometer) and PL (Perkin-Elmer LS55), and LUMO level of MEH-PPV was determined from a CV experimental setup (Autolab PGSTAT30 (Potentiostat)x). The J - V characteristics were examined by a dc power supply (Keithley 2400). Work function of MWCNTs was measured by a photoelectron spectrometer (Riken Keiki, Model AC-2).

I-2 Results and Discussions:

I-2.1 Band Gap Effect

The morphology of (MEH-PPV)-grafted MWCNTs revealed by TEM imaging showed that there were thin coatings, accompanying occasional polymeric particles, on MWCNT surfaces (Figure 10). The particles were attributed to chain branching or crosslinking during graft polymerization. In order to explore the effects of band gap and coating thickness of the grafting MEH-PPV for photocurrent generation, four samples of (MEH-PPV)-grafted MWCNTs of different material parameters were prepared (Table 1). The weight content of the grafting MEH-PPV was determined by TGA analysis (Figure 9), thickness of coating MEH-PPV was determined by TEM images (Figure 10) and TGA analysis, molecular weight was measured by a GPC, and band gap of the grafting MEH-PPV [20] was measured by UV-visible spectra and PL spectra (Figure 8).

For comparison between Sample A and Sample B, (MEH-PPV)-grafted MWCNTs were cast as thin films to examine their *J-V* characteristics in dark and upon illumination. The incident light used in this study (Figure 11) possesses a characteristic spectrum similar to solar spectrum. The intensity was calibrated with the power of 100 mWcm^{-2} by a silicon photodiode. As shown by the *J-V* curves (Figure 4), current under illumination increased about 375-fold in Sample A but only 3-fold in Sample B. This difference arises primarily from the variation of the polymer molecular weight because the weight contents in both cases were almost the identical. As revealed by the color of the emitted light (insets of Figure 4), the band gap of the MEH-PPV is a strong function of molecular weight. By using a Schottky model, this molecular effect can be fully explained. For (MEH-PPV)-grafted MWCNTs, Schottky junctions formed at the MWCNT/MEH-PPV interfaces with MWCNTs being the metallic analogy and MEH-PPV the semiconducting part. The energy band diagram of both Sample A and Sample B are shown in Figure 5 with information of the work function of acid-treated MWCNTs as well as the band gap and LUMO level of the grafted MEH-PPV. As clearly shown in the diagram, electron transfer in Sample A is much more efficient than Sample B, thus resulting significantly greater photocurrent. Specifically, excitons were generated on the MEH-PPV of Sample A (Figure 5a) upon illumination and dissociated at the MWCNT/MEH-PPV interfaces, where electrons were transferred from the conduction band of the grafted MEH-PPV to MWCNTs while the holes stayed behind at the polymer valence band. On the other hand, the photo-excited holes of MWCNTs were injected from MWCNTs to the polymer valence band, forming an effective loop for photocurrents. However, for Sample B, electron transfer was restricted by the energy barrier at the interfaces, thus the holes in polymer valence band transferred to MWCNTs, leading to much lower photocurrents.

	A	B	C	D
Weight content of the grafting polymer	66 wt-%	67.4 wt-%	47.6 wt-%	21.1 wt-%
Thickness of the coating polymer	TEM			
	5.2 nm		4.32 nm	3.63 nm
	TGA			
	33 nm		25.9 nm	20.3 nm
Molecular weight	14.6 K	45.15 K	13.2 K	12.51 K
Band Gap	2.88 eV	2.32 eV	2.89 eV	2.91 eV

Table 1 Four samples of (MEH-PPV)-grafting MWCNTs with different material parameters are used for comparison of the photovoltaic performance.

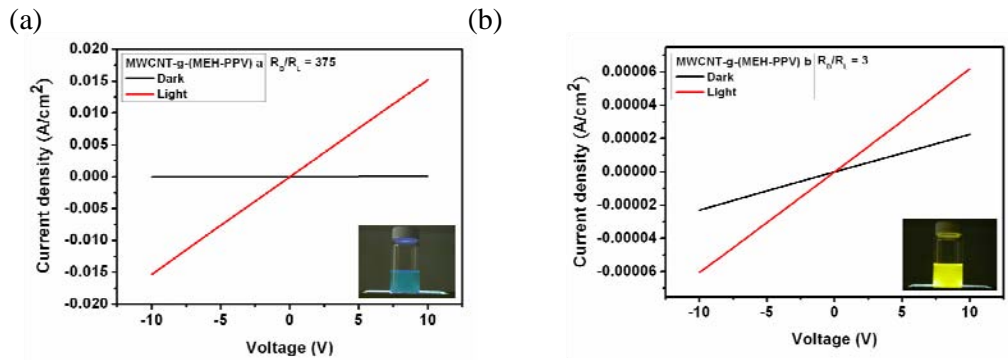


Figure 4 J - V characteristics of (MEH-PPV)-grafted MWCNTs: (a) Sample A and (b) Sample B.

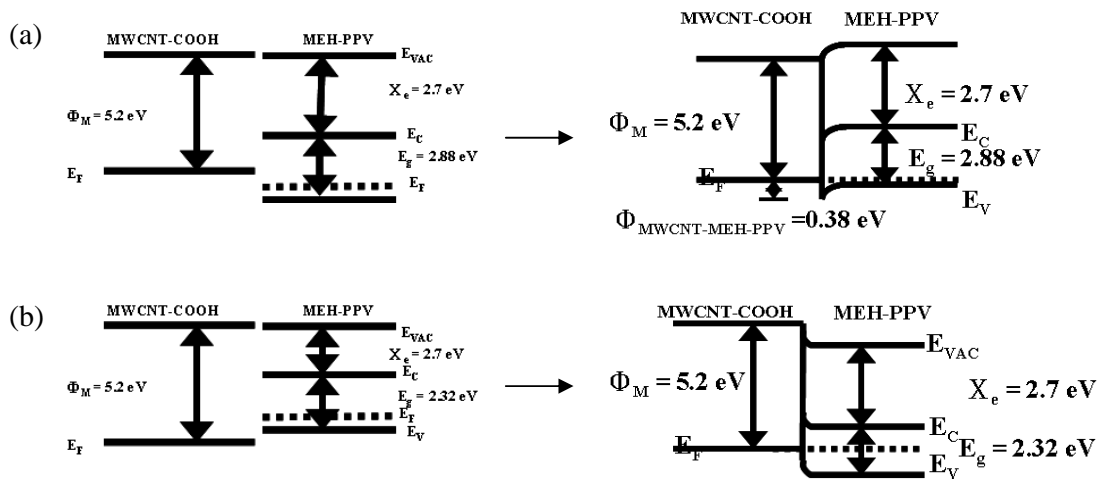


Figure 5 Energy band diagram of the Schottky junctions of (MEH-PPV)-grafted MWCNTs: (a) case a and (b) case b.

I-2.2 Effect of Coating Thickness on CNTs

Compared to Sample A, Sample C and Sample D were prepared with similar molecular weight but different weight fraction of the grafting MEH-PPV. According to UV-visible spectra and PL spectra [20], band gap of the grafting MEH-PPV in these three samples were also similar (Figure 8 and Table 1). The illumination induced photocurrent was measured and shown in Figure 6 with the resistivity detected by a four-point dc probe. The current enhancement, as compared to the dark, was approximately 375-fold, 98-fold and 8.9-fold, respectively, for Sample A, Sample C and Sample D. This indicates that thinner coating MEH-PPV had induced smaller enhancement. Although thicker coating may reduce the electrical conductivity, they also contribute to more exciton generation and reduce the occurrence of short circuit by avoiding contact of neighboring MWCNTs. Nevertheless, new efforts is being undertaken to remove the polymeric particle coating on CNTs (as will be shown later) for more accurate quantitative results.

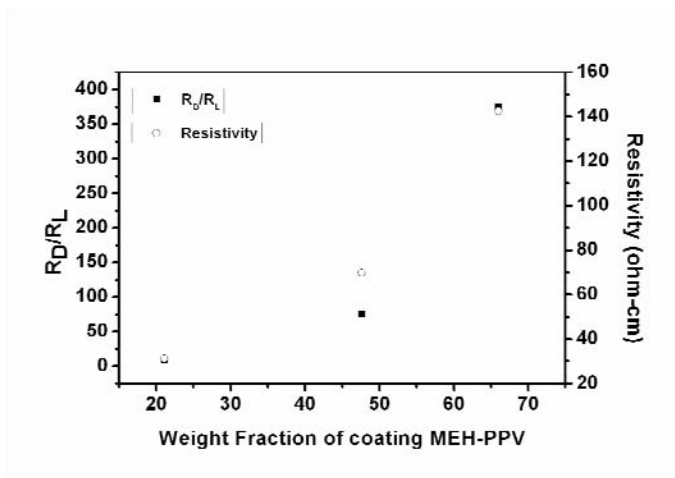


Figure 6 (Left) Current enhancement and (Right) resistivity of (MEH-PPV)-grafted MWCNTs with different weight contents of the grafting MEH-PPV.

I-2.3 Organic Photovoltaic Cell

An organic photovoltaic cell, with (MEH-PPV)-grafted MWCNTs (MWCNT content = 34 wt.%) serving as the photoactive layer, was fabricated and examined for photovoltaic efficiency. As shown by Figure 7, the open-circuit voltage (V_{OC}), short-circuit current density (J_{SC}), fill factor (FF), and power conversion efficiency (η) was 0.355 V, 1.72 mAcm⁻², 0.295, and 0.18% respectively. This result revealed the role of (MEH-PPV)-grafted MWCNTs in the OSCs and have clearly manifested that photocells based on this nanocomposites can provide adequate photo efficiency even when unpackaged at atmosphere. Surface grafting of MEH-PPV on MWCNTs is clearly capable to remove the short circuit problems that were reported before. The device reported here was not yet optimized for the performance and much better

versions are expected there is still ample space for improvement of the photoactive layer.

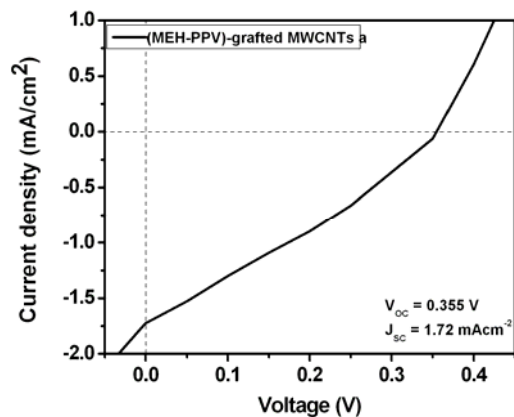


Figure 7 *J-V* characteristics of the organic photovoltaic cell, where (MEH-PPV)-grafted MWCNTs acts as the photoactive layer.

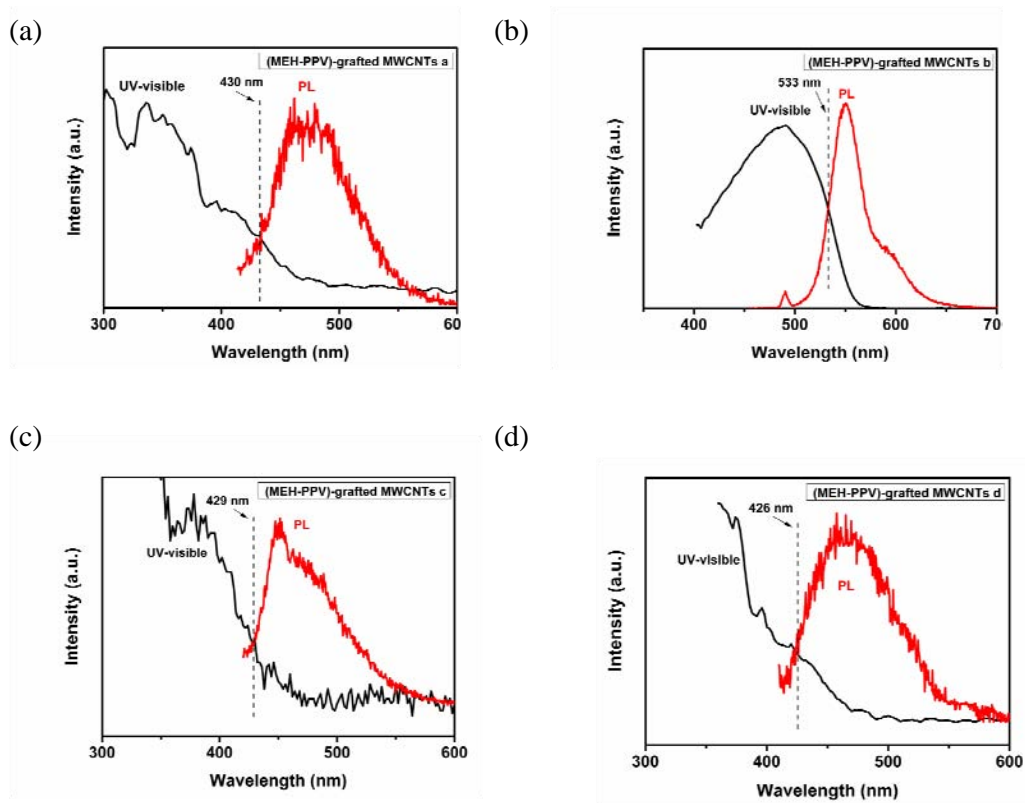


Figure 8 PL spectra and UV-visible spectra of (MEH-PPV)-grafted MWCNTs: (a) case a, (b) case b, (c) case c and (d) case d.

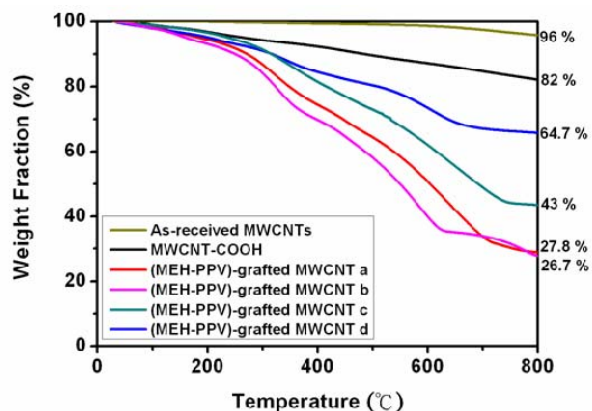


Figure 9 TGA analyses of the as-received MWCNTs, acid-treated MWCNTs and (MEH-PPV)-grafted MWCNTs. Thickness of the grafting MEH-PPV was evaluated by TGA analyses, when (MEH-PPV)-grafted MWCNT was seen as a nanocomposite, where MWCNTs were homogeneously embedded in the MEH-PPV host.

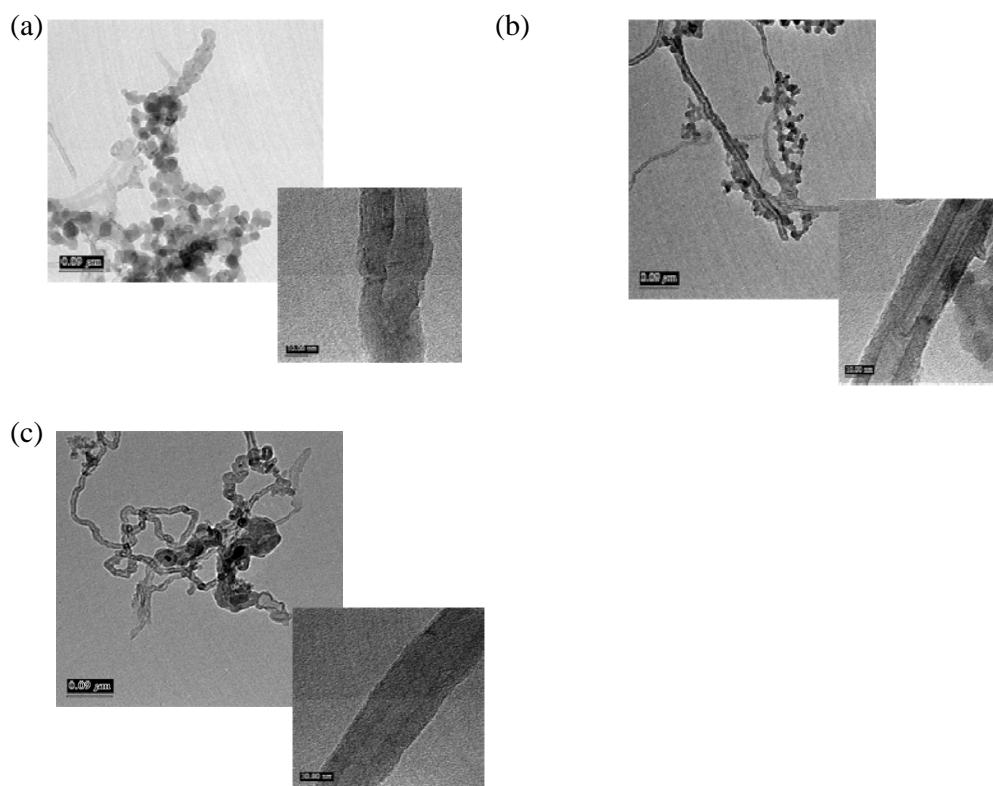


Figure 10 TEM micrographs of (MEH-PPV)-grafted MWCNTs: (a) case a, (b) case c, and (c) case d. Thickness of the grafting MEH-PPV was evaluated by TEM images, which the polymer particles were ignored.

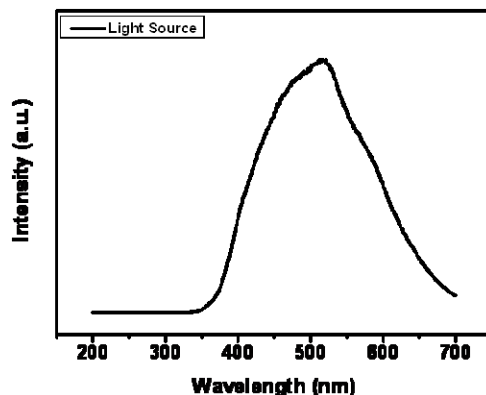


Figure 11. The spectrum of incident light in this study.

I-2.4 Chain conformation of MEH-PPV on MWCNT

In order to explore the chain conformation effect of grafted polymer, the polymeric particles around MWCNTs should be removed. The polymer particles may have gelled during MEH-PPV polymerization²³. The mechanism of gelation in MEH-PPV polymerization was studied by Chun Yin and L. Hontis²⁴⁻²⁵. Wudl and Srdanov were able to minimize the gelation problem by slowly adding excess of the base (t-BuOK).²⁶ Another method reported by B. R. Hsieh is by introducing tert-butylbenzyl chloride into the system to restrain the reaction of gelation²⁷. In this experiment, we have successfully reduced the polymer particles on MWCNTs by decreasing the addition rate of t-BuOK from 0.5ml/s to 0.25ml/s. The PL spectra of these samples were then investigated to reveal the conformation effect on luminescence.

TEM observations:

The TEM photographs of (MEH-PPV)-grafted MWCNTs which were synthesized with slow addition of t-BuOK are showed in Figure 12. From these TEM photographs, we can see that the polymer particles have been removed from the surface of MWCNTs, indicating that gelling of MEH-PPV has successfully restrained. Shown in Figure 13 are the TEM photographs for different reaction times of 4 and 12 hours and the thickness of MEH-PPV coating can be accurately measured to be about 2.9 nm and 4.1 nm, respectively.

TGA data:

From the TGA data (Figure 14), the weight percent of MEH-PPV for the 4 and 12 hours reaction times are approximately 18wt% and 33wt%. The thickness of MEH-PPV coated on MWCNT can be estimated from TGA, the thickness for 4 and 12 hours reaction time are about 2.5 nm and 5.5 nm, respectively.

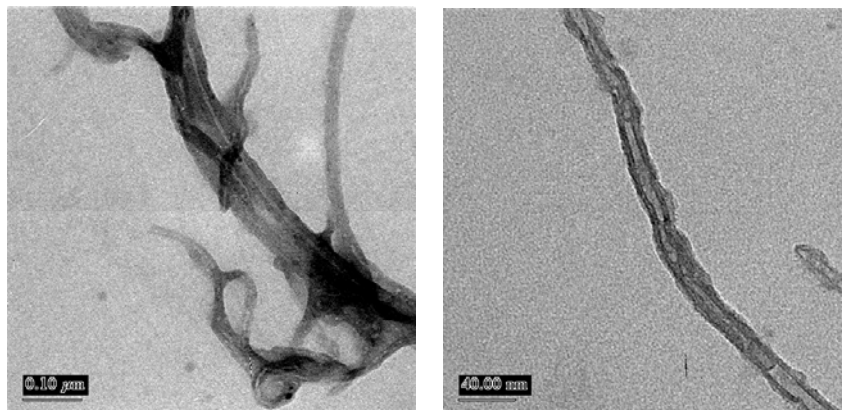


Figure 12. TEM photograph for (MEH-PPV)-grafted MWCNTs

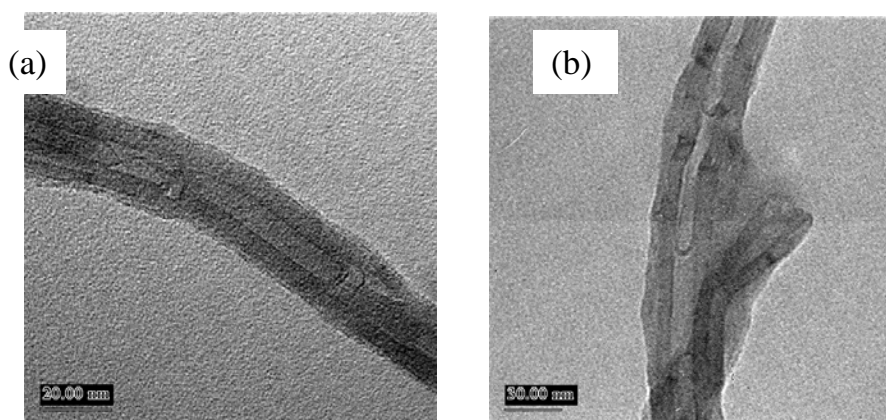


Figure 13. TEM photograph for different reaction time: (a) 4 hours, (b) 12hours

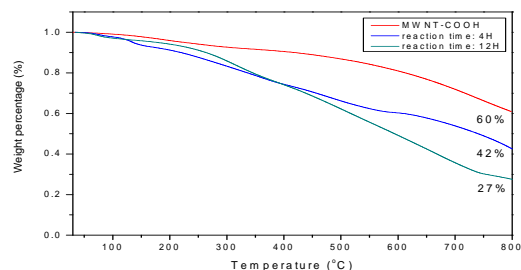


Figure 14. TGA data for different reaction time: (blue) 4 hours, (green) 12hours.

PL spectra:

(MEH-PPV)-grafted MWCNTs were dissolved in THF and PL spectrum was measured by 300nm excitation wavelength (Figure 15). In Figure 15, (MEH-PPV)-grafted MWCNTs demonstrate a luminescence peak at 348nm. Since the

acid-treated MWCNTs and THF do not luminesce with the 300 nm excitation, the luminescence peak at 348nm comes from the MEH-PPV grafted on the MWCNTs.

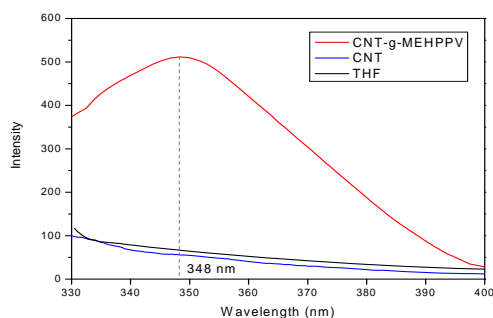


Figure 15. PL spectrum for (MEH-PPV)-grafted MWCNTs, MWCNT and THF

For different reaction times, PL spectra for 4 and 12 hours reaction are showed in Figure 16. The red lines are the spectrums for (MEH-PPV)-grafted MWCNTs and the blue lines are the spectrums of MEH-PPV which were cut from MWCNT by KOH refluxing. We can see that the peaks red-shift from 348nm to 409nm after MWCNTs were separated from MEH-PPV. It means that the presence of MWCNTs will affect the spectrums of MEH-PPV. The change of the spectrum for MEH-PPV represents that the conjugated length are changed by MWCNT, or the conformation are affected by MWCNT.

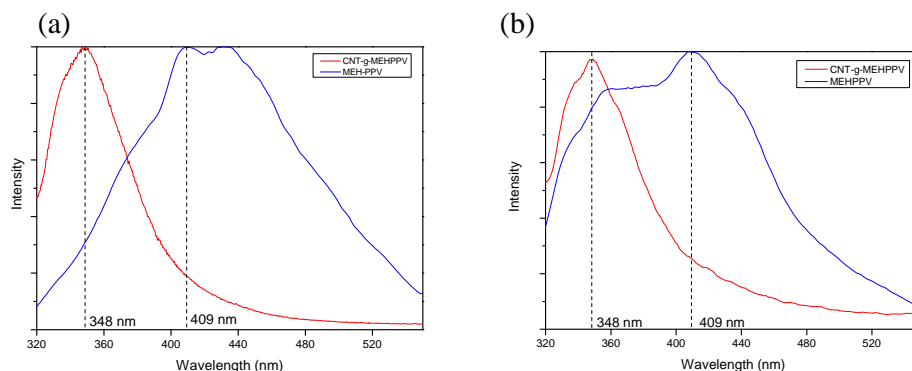


Figure 16. PL spectrum for different reaction times: (a) 4 hours, (b) 12hours

Zhenwei Wang and B. McCarthy found that the spectrum of conjugated polymers blue-shifts after introducing the MWCNT into polymer solution without covalent bonding²⁸⁻³⁰. According to the previous research, because there are aromatic rings on the backbone of PPV, the interaction between polymer and MWCNT is very strong. This strong interaction prompts PPV to attach on the surface of MWSNT³¹. This was verified via Raman spectrum observation by McCarthy²⁹. To explain the blue-shift

phenomenon, Ago et al. suggested that CNT provide a cylindrical surface for polymer to bind, and the conjugated length of polymer will be decreased. Thus the spectrums of conjugated polymer will blue-shift after introducing CNT into polymer system. In our system, since the MEH-PPV is bonded around MWCNTs via covalent bonding, MEH-PPV will have stronger interaction with MWNTs. Therefore, the PL spectrum will blue-shifted significantly.

I-3. Conclusions:

A novel material, (MEH-PPV)-grafted MWCNTs, was synthesized via a surface grafting method. Surface grafting of MEH-PPV to MWCNTs showed significant photocurrents excited upon illumination. TEM micrographs revealed a firm coating MEH-PPV on the MWCNT surface and the weight fractions of MEH-PPV were estimated by TGA analyses. By tuning experimental parameters, different weight fractions and different molecular weight of MEH-PPV were grafted to MWCNTs to explore the observed effects of band gap and coating thicknesses. A Schottky model was used to interpret the observed effect due to variation of the band gap of MEH-PPV and PET. The Schottky junctions formed at the MWCNT/MEH-PPV interfaces and the appropriate band gap would make PET more efficiently. Effect of coating thicknesses of MEH-PPV was also observed, in which thicker MEH-PPV layers resulted in larger enhancement of current and decreased the occurrence of short circuit. With the (MEH-PPV)-grafted MWCNTs served as the photoactive layer, an organic photovoltaic cell was fabricated. The V_{OC} , J_{SC} , FF and power conversion efficiency of the OSC were 0.355 V, 1.72 mAcm⁻², 0.295, and 0.18%, respectively. These results strongly indicate that grafting MEH-PPV to CNTs can effectively inhibit short circuiting, thus, combining the other unique advantages of these nanocomposites, ultra-high load of MWCNTs and (MEH-PPV)-grafted MWCNTs may be promising materials to be used in organic photovoltaic cells.

The gelling problems of (MEH-PPV)-grafted MWCNT can be removed by slow addition of t-BuOK (0.25mg/l/s). The strong interactions between MEH-PPV and CNTs have created tightly attached MEH-PPV layer on MWCNT, leading to decrease of the conjugated length of MEH-PPV and blue-shift of the PL spectrums from 409nm to 348nm.

References

1. S. Iijima, *Nature* **1991**, 354, 56-58.
2. J.W. Mintmire, C.T. White, *Carbon* **1995**, 33, 893-902.
3. P. Poncharal, Z.L. Wang, D. Ugarte, W.A. de Heer, *Science* **1999**, 283, 1513-1516.
4. R.S. Ruoff, D.C. Lorents, *Carbon* **1995**, 33, 925-930.

5. M.M.J. Treacy, T.W. Ebbesen, J.M. Gibson, *Nature* **1996**, *381*, 678-680.
6. E.W. Wong, P.E. Sheehan, C.M. Lieber, *Science* **1997**, *277*, 1971-1975.
7. X.W. Jiang, Y.Z. Bin, M. Matsuo, *Polymer* **2005**, *46*, 7418.
8. Z. Ounaies, C. Park, K.E. Wise, E.J. Siochi, J.S. Harrison, *Compos Sci Technol* **2003**, *63*, 1637.
9. Y.Z. Long, Z.J. Chen, X.T. Zhang, J. Zhang, Z.F. Liu, *J Phys D Appl Phys* **2004**, *37*, 1965.
10. R. Martel, T. Schmidt, H.R. Shea, T. Hertel, Ph. Avouris, *Appl. Phys. Lett.* **1999**, *73*, 2447.
11. R.D. Antonov, A.T. Johnson, *Phys. Rev. Lett.* **1999**, *83*, 3274.
12. X. W. Jiang, Y. Z. Bin, M. Matsuo, *Polymer* **2005**, *46*, 7418.
13. C. Yang, M. Wohlgenannt, Z.V. Vardenya, W.J. Blau, A.B. Dalton, R. Baughman, A.A. Zakhidov, *Physica B* **2003**, *338*, 366-369.
14. S.A. Curran, P.M. Ajayan, W.J. Blau, D.L. Carroll, J.N. Coleman, A.B. Dalton, A.P. Davey, A. Drury, B. McCarthy, S. Maier, A. Strevens, *Adv. Mater.* **1998**, *10*, 1091.
15. H. Ago, M. Shaffer, D. Ginger, A. Windle, R.H. Friend, *Phys. Rev. B* **2000**, *61*, 2286.
16. D.M. Guldi, G.M.A. Rahman, F. Zerbetto, M. Prato, *Acc. Chem. Res.* **2005**, *38*, 871.
17. B. Pradhan, S.K. Batabyal, A.J. Pala, *Appl. Phys. Lett.* **2006**, *88*, 093106.
18. B.J. Landi, R.P. Raffaele, S.L. Castro, S.G. Bailey, *Prog. Photovolt: Res. Appl.* **2005**, *13*, 165-172.
19. J.A. Rud, L.S. Lovell, J.W. Senn, Q. Qiao, J.T. Mcleskey, *J. Mater. Sci.* **2005**, *40*, 1455.
20. M. Fox, *Optical Properties of Solids*, Oxford, **2001**, 173-176.
21. Z. Ounaies, C. Park, K.E. Wise, E.J. Siochi, J.S. Harrison, *Compos. Sci, Technol.* **2003**, *63*, 1637.
22. Y. Z. Long, Z. J. Chen, X. T. Zhang, J. Zhang, Z. F. Liu, *J. Phys. D Appl. Phys.* **2004**, *37*, 1965.
23. F. Wudl, P. M. Allemand, G. Srdanov, Z. Ni, D. Mcbranch, *ACS Symp. Series* **1991**, *455*, 683-686.
24. C. Yin, C. Z. Yang, *J. Appl. Polym. Sci.* **2001**, *82*, 263-268.
25. L. Hontis, M. Van der Borgh, D. Vanderzande, J. Gelan, *Polymer* **1999**, *40*, 6615-6617.
26. F. Wudl, G. Srdanov, U.S., 1993; Vol. Patent 5, p 136
27. B. R. Hsieh, Y. Yu, A. C. VanLaeken, H. Lee, *Macromol.* **1997**, *30*, 8094-8095.
28. Z. Wang, C. L. Liu, Z. G. Liu, H. Xiang, Z. Li, Q. H. Gong, *Chem. Phys. Lett.* **2005**,

- 407, 35-39.
29. B. Mc Carthy, A. B. Dalton, J. N. Coleman, H. J. Byrne, P. Bernier, W. J. Blau, *Chem. Phys. Lett.* **2001**, 350, 27-32.
 30. B. McCarthy, J. N. Coleman, R. Czerw, A. B. Dalton, M. I. H. Panhuis, A. Maiti, A. Drury, P. Bernier, J. B. Nagy, B. Lahr, H. J. Byrne, D. L. Carroll, W. J. Blau, *J. of Phys. Chem. B* **2002**, 106, 2210-2216.
 31. M. J. Yang, V. Koutsos, M. Zaiser, *J. of Phys. Chem. B* **2005**, 109, 10009-10014.

Chapter II

Single-molecule luminescence of conjugated polymers

II-1 Strain-induced dramatic enhancement of single-molecule luminescence of conjugated polymers by nano-plastic flows

Although a number of studies for devices based on MEH-PPV have been performed to control the overall functions, crucial factor arising from exciton-exciton annihilation and interchain interactions between polymer chains cannot be excluded in the solid films or in high-concentration solutions¹. These chain packing induced behaviors strongly affect the electronic properties of this material, especially the carrier mobility in polymers. For example, the presence of interchain interactions has important implications for conjugated polymer-based LEDs. Increased interchain interactions promote charge transport but also lower the luminescence quantum efficiency². Schwartz et al. had also proposed that the existence of interchain interaction is directly connected to the film morphology^{3, 4}. The morphology of spin-cast polymer thin films can be altered by changing the solvent or the polymer concentration of the solution from which the film is cast or by changing the spin speed, etc.... All the sample preparation methods above will also affect the interchain interaction behavior.

There are some methods had been proposed to reduce the behaviors of interchain interactions. One of the system have been adapted is the blends of conjugated polymers with saturated polymers^{2, 5, 6}. It is generally believed that the conjugation segments aggregate in thin film when the concentration of conjugated polymers in increased. As a result, when the host matrix of the blend is the saturation polymer, and the guest component is the conjugated polymer, we can effectively reduce the interchain interactions by increasing the physical separation between the individual conjugated polymer chains. This behavior is so called “dilution effect” has been showed in the MEH-PPV/PS blending system, too⁷⁻¹⁰.

In this article, the blending system has been adapted because of their improving optoelectronic properties⁷⁻¹⁰. On the other hand, for further studying how the behaviors of chain packing will affect its optical properties, we observe the crazing behaviors of this kind of un-crosslinked thin film by introducing the tensile test on the copper grid bonded with thin film. The crazing micro-mechanism of polymer thin film has also been studied extensively¹¹⁻¹⁶. It is believed that the brittleness properties of glassy polymers could be traced to the forming of the crazes when undergo plastic deformation¹⁷⁻²⁷. When the craze grow, no only the craze tip advances, but the craze

get thicken at the craze-matrix interface. During craze thickening, the new material (polymers in the matrix) is drawn into the craze region from the elastic region (the polymer outside the craze is assumed to be under linear elastic deformation). In the craze region, there is a remarkable value of draw ratio has been measured by the TEM micro-densitometry technique, namely $\lambda_{\text{craze}}=400\%$ ($\epsilon=300\%$)^{14-16, 23}. This amazing value of draw ratio is much larger than the elongation in bulk polymer material. From this special micro-mechanism, we can further exam the chain's behavior of conjugated polymer, and how this behavior will affect the luminescence property of conjugated polymer.

II-1.1 Experimental Procedures:

The MEH-PPV we used was purchased from Sigma-Aldrich Chemical Co. with average number molecular weight $M_n=150,000\sim 250,000$ g/mol and molecular weight dispersity $M_w/M_n \approx 5$. The polystyrene (PS) we used was purchased from the Pressure Chemical Co. with $M_w=2M$ and molecular weight dispersity $M_w/M_n \leq 1.30$. Both MEH-PPV and PS was used as received without further purification.

Different weight percentage of both material blending solutions were prepared, namely 0.1wt% MEH-PPV (99.9wt% PS), 0.5wt% MEH-PPV (99.5wt% PS), 1wt% MEH-PPV (99wt% PS), 5wt% MEH-PPV (95wt% PS), and 10wt% MEH-PPV (90wt% PS) respectively. The concentration of all the solutions above is 25mg (weight of MEH-PPV + PS)/ml (solvent). The solvent we used is the mixture of toluene THF and Cyclohexanone with the same volume percentage. These solutions were stirred for a minimum of 48h at 50°C from the beginning they have been prepared.

The polymer thin film was prepared by solution-casting the blending solution in a spin coater at spin speed of 2500 rpm ~ 3000 rpm on glass slides, and the film thickness was well controlled to be around 0.5 μm (decided by α -step). When the solvent evaporated, the blending film was floated off the slides onto a surface of DI water bath and picked up on a piece of copper grids which have been annealed at 600°C for 1h and pre-coated with PS from PS (2M) solutions. After the copper grid with thin film was dried for about 24h, the film was briefly exposed to the vapor of solvent, which was used to prepare our solution, to bond the film to the copper grid (over-solvent process). The specimen was then mounted in a strain jig and stretched under an optical microscope to observe the formation and the growth of crazes. The stretched samples were then examined by photo-luminescence spectrophotometer (Perkin-Elmer LS-55), atomic force microscope (Digital Instrumental, Nanoscope IIIa DimensionTM 3100) and transmission electron microscope (JEOL JEM-2010 TEM) to evaluate its photo-luminescence intensity, the topography and internal structure of crazes.

Except for the crazing behavior of MEH-PPV/PS (2M) blending specimens, we also observed the behavior of uniform deformation and shear deformation zone by MEH-PPV/PS (30wt%2M + 70wt%760) [PS (760) was purchased from the Pressure Chemical Co. with $M_w = 760$ and molecular weight dispersity $M_w/M_n \leq 1.13$] and MEH-PPV/PPO (PPO we used was purchased from Sigma-Aldrich Chemical Co. with average number molecular weight $M_w = 244,000$ g/mol) blends respectively. All the experiment procedure is the same with the MEH-PPV/PS (2M) system, the only differences are that the MEH-PPV/PPO solutions were stirred for a minimum of 24h at 70°C from the beginning they have been prepared and the thin film of MEH-PPV/PPO must keep in the atmosphere for 2 weeks to form the structure of shear deformation zones (SDZs) under stretching, otherwise the deformation of thin film will be uniform²⁸. On the other hands, the 0.5wt% MEH-PPV/PS (2k+2M with the same weight fraction) [PS (2k) was purchased from the Pressure Chemical Co. with $M_w = 2032$ and molecular weight dispersity $M_w/M_n \leq 1.06$] blending thin films were also prepared to verify the midrib behaviors of the crazes.

II-1.2 Results and Discussions:

Figure 1(a) shows the PL emission spectra for a series of different MEH-PPV/PS (2M) blends with no deformation ($\epsilon=0$). As can be seen, the emission spectra of MEH-PPV/PS blends show strong concentration dependence. All the PL emission spectra show two obviously emission peak around 550nm and 590nm respectively. As shown in Figure 1(a), the intensity of the 550nm relative to the 590nm diminishes with increasing MEH-PPV concentration, and we can reasonably speculate that for pure MEH-PPV thin film, the peak of 590nm will dominate the whole spectra and the peak at 550nm will disappear. In normalized spectra which were normalized with the corresponding contents of MEH-PPV in blends, just like the inset of Figure 1(b), the enhanced PL efficiency is observed in the very dilute situation. Both phenomena above can be explained by the existence of PS dramatically reduced the interchain interaction between conjugated polymer chains^{7, 9, 10}. Since the MEH-PPV chains are separated by the inert PS in the blends, the conjugation segments form a separated state and thus emission mainly originates from optical transition of the excitons in the separated state. It had also be previously discovered that the isolated MEH-PPV chains (even in dilute solution or blends), can produce the intrachain singlet excitons, which are formed in high quantum yield²⁹. Thus, the 550nm emission peak can be attributed to the intrachain emission. As increasing the content of MEH-PPV in blends, the physical distance between MEH-PPV chains decrease so that the conjugated segments in the different chains come together to form aggregated state. With the gradually increased emission peak around 590nm, we can conclude that the 590nm emission is due to the

aggregated state. On the other hand, the enormous efficiency enhanced with the reduced content of MEH-PPV is also due to the reducing the non-emissive excitons analogous to charge transfer between different chains. All these behaviors are similar to the previously studies and named “dilution effect”.

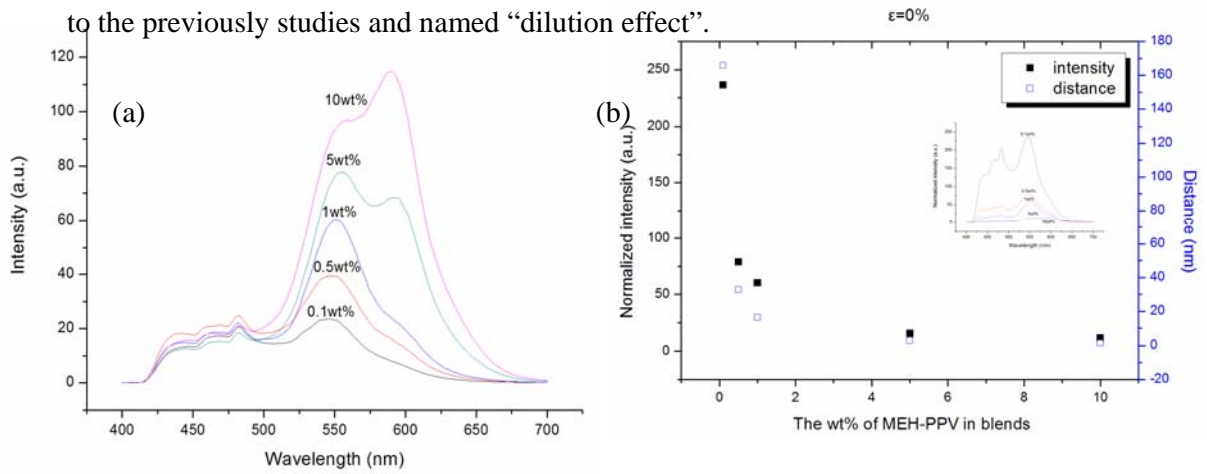


Fig. 1 (a) PL spectra of MEH-PPV/PS (2M) blends for different contents of MEH-PPV in blends. (b) Plot for values of normalized intensity and the distances between coils of MEH-PPV with respect to the different MEH-PPV contents. The inset shows the PL spectrum normalized with the contents of MEH-PPV for each blend. (Note: the peaks of PL spectrums near the 400nm-500nm are due to the existence of cooper grid, the following PL spectra are under the same consideration.)

With the continuously stretching test that the crazing behavior appeared, and the following record of the PL spectra with different degree of stretching, something interesting had been found. For the concentrations of MEH-PPV were 0.1wt%, 0.5wt%, and 1wt%, the obviously enhancement of PL intensity during the stretching process was observed [Figure 2(a), (b), (c)]. From these spectra which were under the same operational parameter, we can clearly find that the PL intensity of samples stretching to $\epsilon=24\%$ is more than twice of the un-stretching samples, and there are not obviously wavelength shift during the stretching process. However, this kind of phenomena was not obvious for the contents of MEH-PPV are 5wt% and 10wt%. For these two cases, even the crazing behaviors are similar with the other groups [0.1, 0.5, 1wt% MEH-PPV/PS (2M)], but no PL intensity enhancement was observed during the stretching process.

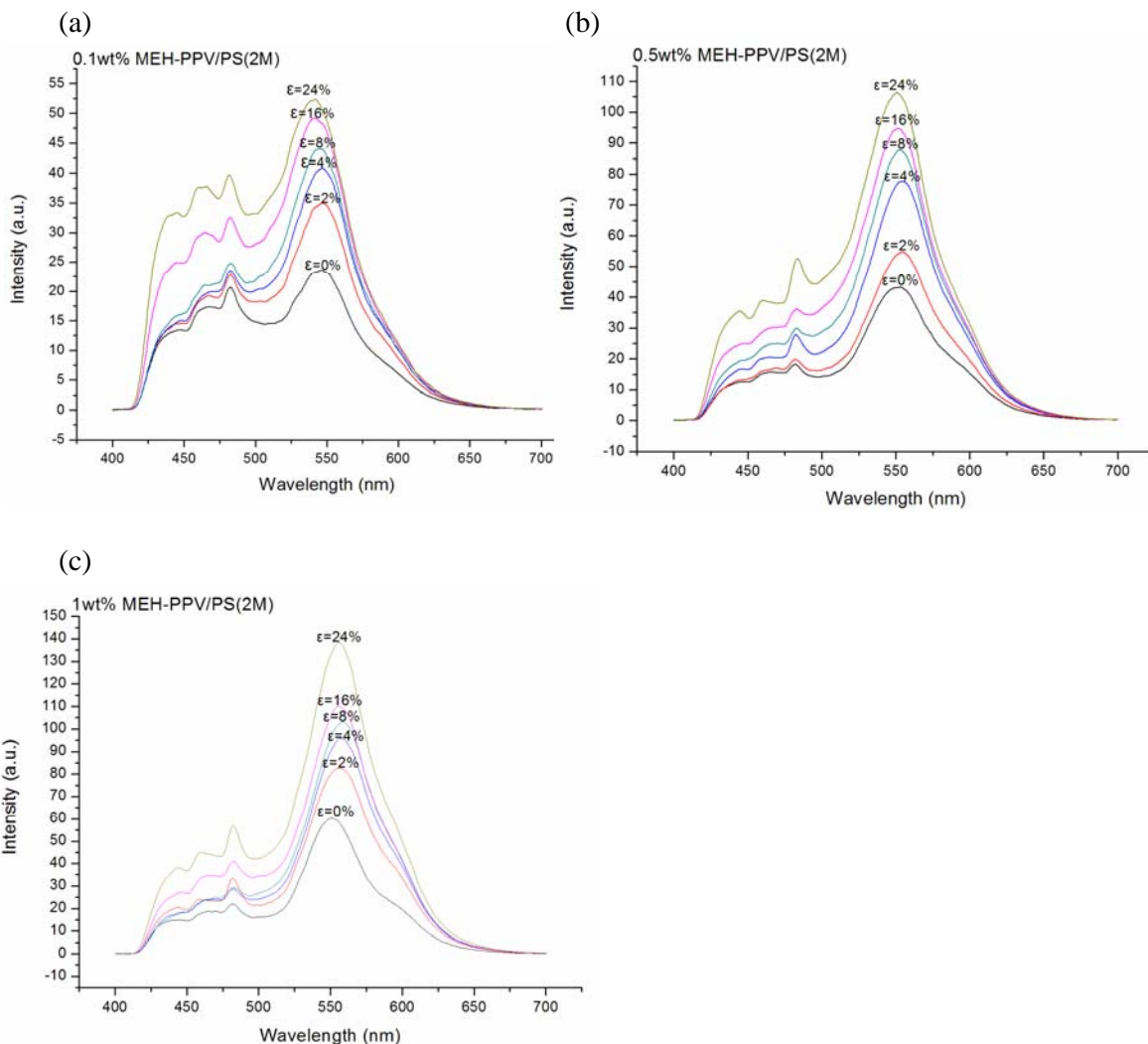


Fig. 2 PL spectra for different stretching state of (a) 0.1wt% MEH-PPV/PS (2M), (b) 0.5wt% MEH-PPV/PS (2M) and, (C) 1wt% MEH-PPV/PS (2M).

To verify if the appearance of crazes will actually affect the PL performance, the PS (2M) was replaced by (1) PS (760) + PS (2M) and (2) PPO respectively. Under the same experimental procedures and techniques, the MEH-PPV/PS (2M + 760) blends express the uniform deformation behaviors and the MEH-PPV/PPO blends show the structure of shear deformation zones after stretching. For the MEH-PPV/PS (2M + 760) blends, we can still observe the obviously dilution effect before the stretching for different contents of MEH-PPV [Figure 3(a), (b)] just like previously descriptions, but there are no intensity enhancement phenomena when the films undergo a uniform deformation in the continuous stretching course for all sets of the blends (0.1wt%, 0.5wt%, 1wt%, 5wt%, 10wt% of MEH-PPV) even the strain value was achieved to

$\varepsilon=20\%$. On the other hands, the MEH-PPV/PPO blends show some special manifestation. If we proceeded the stretching right after the step of over-solvent, the thin film would undergo a uniform deformation, but if we aged the samples in the atmosphere for about 2 weeks (or heating under 120°C for 1 hr), the shear deformation zones (SDZs) would show up after stretching²⁸. Here, both uniform deformation and SDZs circumstances were studied and their PL behaviors didn't show serious differences. Just like the Figure 4(a), (b), the un-stretched samples of different contents of MEH-PPV didn't show the dilution effect, namely neither wavelength shift for different contents of MEH-PPV nor intensity enhancement for very dilute situation. By the way, the position of main peak is near the 580nm which is also different from the MEH-PPV/PS blends. After stretching, the PL intensity didn't show obviously change just like the MEH-PPV/PS (2M+760) case no matter if the SDZs would show up. So we can probably make sure that the PL intensity enhancement behavior is strongly related to the forming of crazes.

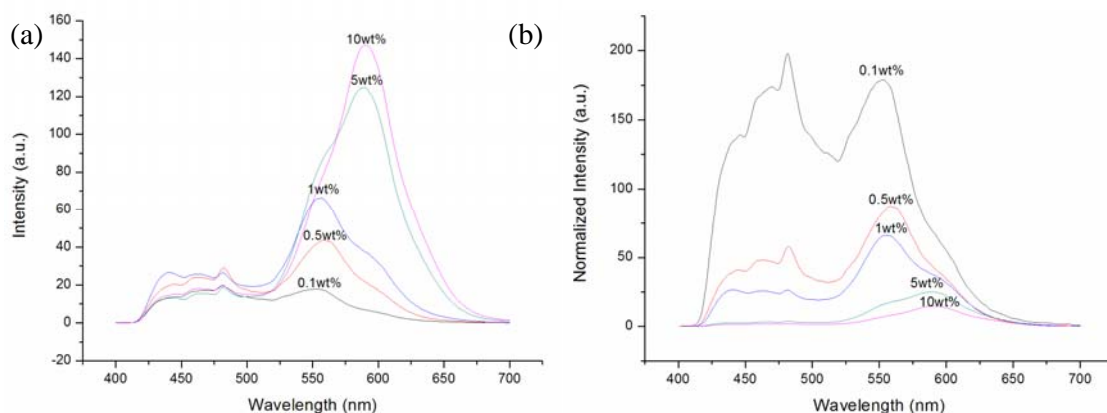


Fig. 3 PL spectra of MEH-PPV/PS (2M + 760) blends for (a) different contents of MEH-PPV in blends, and (b) normalized to the different MEH-PPV contents.

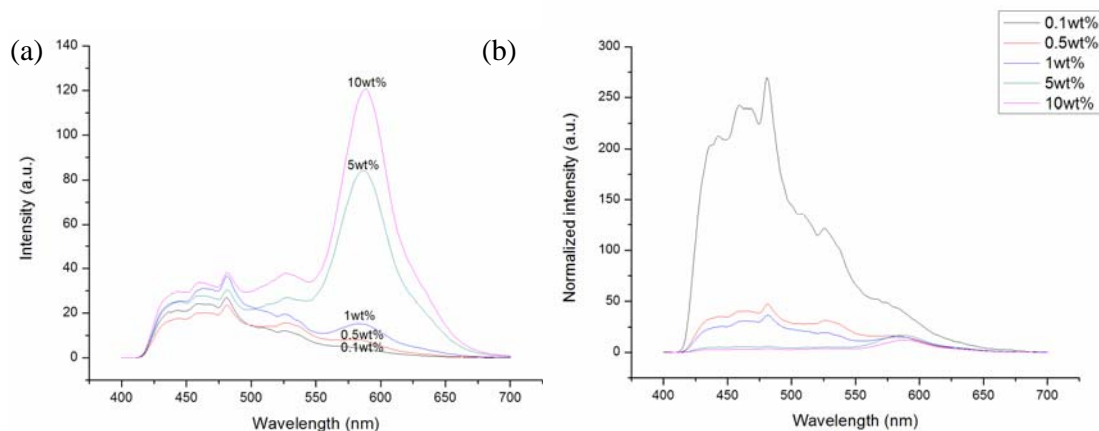


Fig. 4 PL spectra of MEH-PPV/PPO blends for (a) different contents of MEH-PPV in

blends, and (b) normalized to the different MEH-PPV contents.

From the well known knowledge about the crazes, we know that when the crazes show up in PS thin film, the strain in the crazes would reach an amazing value, namely $\varepsilon=300\%$. This astonishing deformation is much larger than the situation of bulk, and we could reasonably image that under such huge deformation, something would be very difference from the normal thin film. We had already known that if we can effectively reduce the interchain interaction, we can enhance the luminescence efficiency remarkably. We also know that these kinds of chain packing induced drawbacks can be improved by the physical separation of conjugated polymer chains. As a result, when the conjugated polymer chains are tolerated such a dramatically deformation in the crazed region, do the distances between the conjugated polymer chains increase to achieve the effect of physical separation, and further improve our PL Intensity? Figure 5 shows the diagrams of the depth versus width recorded by AFM of the different crazes for different contents of MEH-PPV in MEH-PPV/PS (2M) blends. With the increased contents of MEH-PPV, the saturation depths³⁰ of the crazes decreased also the slope of linear growth region (Figure 6). From these observations, we can almost confirm that the chains of MEH-PPV do exist in the crazes because in certain degree, the rigid rod-like MEH-PPV chains effectively restrict the growth of crazes. If the crazes didn't contain the chains of MEH-PPV, namely the forming of crazes were all contributed by the saturated polymer, PS, the growth of crazes would show similar behaviors, for example, the ratio of depth to width. For the reasons above, the chains of MEH-PPV considerably sustained the enormous strain in the craze. Under such assumptions, and some known physical parameters, we can probably estimate the physical separation of the individual MEH-PPV polymer chains. Figure 7 (a) shows the chemical structure of MEH-PPV, and the monomer molecular weight (M_0) of MEH-PPV could be easily calculated, namely 260 g/mol. From

$$R_G^2 = \frac{n_k b_k^2}{6} = \frac{l_p L}{3} = \frac{l_p \frac{M_w}{M_0} 0.6}{3}$$

where n_k is the number of kuhn monomers, b_k means the length of the kuhn monomers, l_p represents the persistence length, L is the contour length of a single chain, and M_w is the molecular weight, we can get the R_G for our MEH-PPV molecular [the persistence length (l_p) for MEH-PPV is 6.0 nm³¹], e.g. 26.312~33.968nm. Here the length of PPV monomers were adapted, namely 0.6nm³¹. Then the c^* could be calculated by

$$c^* = \frac{M_w}{\frac{4\pi R_G^3}{3} N_{AV}}$$

The c^* is equal to 2.529~3.266 mg/ml for our MEH-PPV. The same method could be

adapted to calculate the R_G of PS (2M), namely 38.7298nm. From the discussions above, the R_G for MEH-PPV and PS (2M) were similar under our experimental parameter (the thickness of our thin films are 0.5 μ m). As a result, we assume the molecular chains of both MEH-PPV and PS (2M) were under the similar deformation. Next, the PS (2M) was further took as solvent for MEH-PPV in the blending thin films. By this assumption, we could transfer the units of different contents of MEH-PPV from weight percentage to concentration through the density of PS (2M) [$\rho=1.04\sim 1.065$ g/ml for PS] (Table 1). The R_G for our MEH-PPV had been carried out from the above calculation, for convenience, the average value, $R_G = 30.14$ nm, was adapted to our following calculation. We know that under theta condition, ($c=c^*$), the distance between the centers of two molecular coils would equal to $2R_G$ in the solution state (Figure 8). Because the PS (2M) was taken as the solvent, we could estimate the distance between the centers of molecular coils for MEH-PPV in different solution-liked concentration cases got from Table 1 approximately by

$$l_0 = \frac{2R_G c^*}{c}$$

where l_0 is the distance between the centers of MEH-PPV coils apart from the c situation.

	0.1wt%	0.5wt%	1wt%	5wt%	10wt%
	MEH-PPV/PS (2M)				
c =weight of MEH-PPV/volume of PS (2M) (mg/ml)	1.041~1.065	5.228~5.352	10.505~10.758	54.737~58.053	115.559~118.333

Table1. The concentrations of MEH-PPV in the different blending thin films which took PS as the solvent.

	0.1wt%	0.5wt%	1wt%	5wt%	10wt%
	MEH-PPV/PS (2M)				
l_0 (nm)	165.7846	33.0242	16.4291	3.1531	1.4936

Table2. The distances between the centers of MEH-PPV coils for different MEH-PPV/PS (2M) blends before stretching.

(a)

(b)

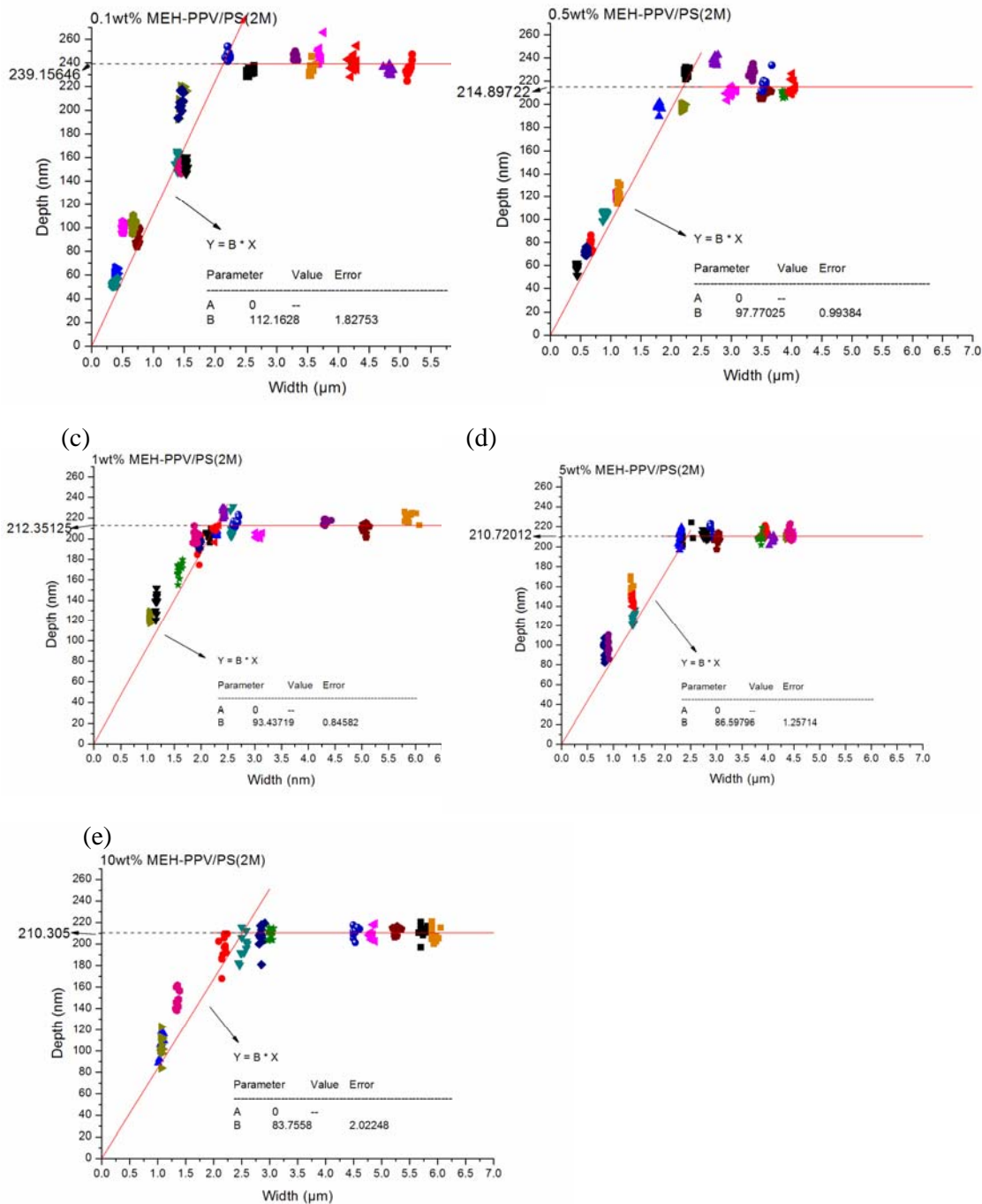


Fig. 5 The diagrams of depth versus width of different crazes for (a) 0.1wt% MEH-PPV/PS (2M), (b) 0.5wt% MEH-PPV/PS (2M), (c) 1wt% MEH-PPV/PS (2M), (d) 5wt% MEH-PPV/PS (2M), (e) 10wt% MEH-PPV/PS (2M) blends. The “B” represents the slope for the region of linear growth. (Note: the main peak of normalized spectrum for 0.1wt% in Figure 5(b) is higher than the others. This may be due to the peaks near the 400nm-500nm spread into the position of the main peak.)

Table 2 concludes the value of l_o for different MEH-PPV/PS (2M) blends. We had

mentioned that in the craze region, there is a remarkable value of draw ratio has been measured by the TEM micro-densitometry technique, namely $\lambda_{\text{craze}}=400\%$ ($\varepsilon=300\%$). Now, the distance between coils to coils of MEH-PPV for un-stretched situation had been decided (l_0), and the distance after the crazes showed up could be evaluated by

$$l = \varepsilon l_0 + l_0$$

where l is the distance between the centers of coils for MEH-PPV after the forming of crazes.

Table 3 shows the final results of calculation, and we can figure out that for the low concentration cases, e.g. 0.1wt%, 0.5wt%, 1wt%, the distances between coils to coils of MEH-PPV molecules are larger than $2R_G$ after the appearing of crazes. For the 5wt% and 10wt% cases, the calculated values of l are lower than the $2R_G$. As a result, we proposed that when the contents of MEH-PPV are as low as some critical value, the enormous strain in the crazes would separate the MEH-PPV polymer chains and further enhanced its PL efficiency, on the other hands if the concentration of MEH-PPV in the blends is too high, even the craze showed up, the physical distances between the polymer chains are not enough to suppress the interchain interaction. This hypothesis exactly matches our experiment results, e.g. during stretching process, the samples which exist the crazing behaviors for low contents of MEH-PPV showed obviously behaviors of intensity enhanced, but not for the high concentration parts. Figure 1(b) also showed the diagram of distances between molecular coils for MEH-PPV molecules versus the contents of MEH-PPV in blends at non-stretched situation ($\varepsilon=0$). The normalized intensity for different blends showed similar trends with the distances between MEH-PPV coils. For the cases that had tolerated some degree of strain (e.g. $\varepsilon=2\%$, 4%, 8% 16% and 24%), they also showed the similar trends just like the un-stretched situation (data had not showed). From this aspect, the physical separation of individual conjugated polymer chain did have some relationship with its luminescence efficiency. Return to the other two experiments, e.g. MEH-PPV/PS (2M+760) and MEH-PPV/PPO, which either showed the uniform deformation or SDZs, the strain for the uniform formation of MEH-PPV/PS (2M+760) or MEH-PPV/PPO was almost equal to the applied strain of strain jig and for SDZs formed by stretching the PPO was about 60%³². These strains were too small to separate our molecular chains of MEH-PPV, so the experiment results which didn't show any enhancement of PL intensity also harmonized to our estimates.

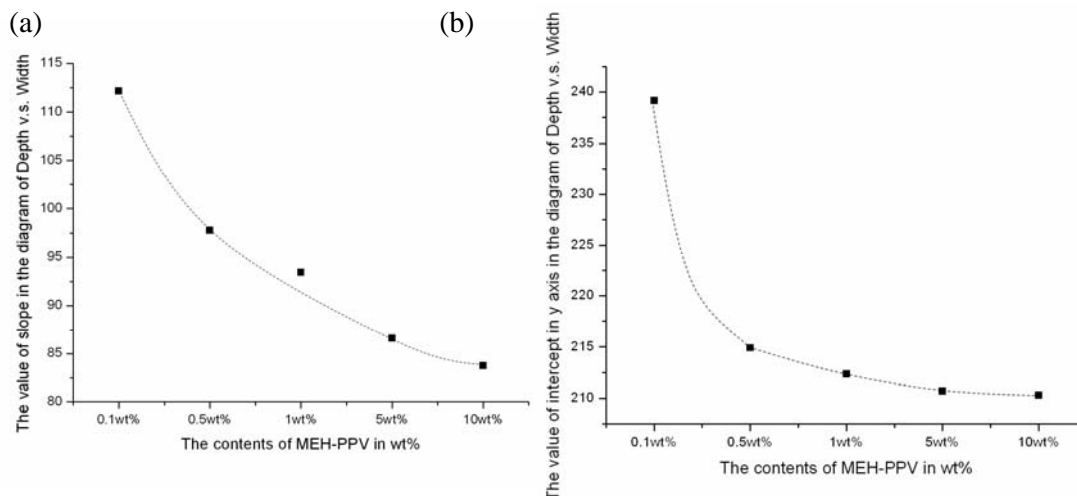


Fig. 6 The (a) slope and (b) intercept of y axis in the diagram of depth versus width for different crazes.

	0.1wt% MEH-PPV/PS (2M)	0.5wt% MEH-PPV/PS (2M)	1wt% MEH-PPV/PS (2M)	5wt% MEH-PPV/PS (2M)	10wt% MEH-PPV/PS (2M)
l (nm)	663.1383	132.0966	65.7164	12.6122	5.9742

Table3. The distances between the centers of MEH-PPV coils for different MEH-PPV/PS (2M) blends after the crazes showed up.

On the other hand, the value of l_0 for the 0.1wt% MEH-PPV/PS (2M) blends had already exceeded the value of $2R_G$ but it still showed strong enhancement of PL intensity after stretching. These could be due to the suppressions of structural defects which introduced deep levels through within the energy gap after the polymer chain had been drawn into the crazed region and formed the fibrils. Meng and Hong had proved that the origin of photoconductivity in conjugated polymers is mainly came from the quenching of currieries through structural defects which introduce deep levels within the energy gap. If the exciton binding energy is smaller than the deep level binding energy, the electron of the exciton can drop into the deep level through multi-phonon emission while the hole is released to be the free carrier when the level is initially empty³³. In other words, we can say that the formation of exciton or combination of electrons and holes which will cause the emission of energy by the radiation form will proceed more easily if the structural defects are reduced. Under continuous stretching, the polymer chains in the fibrils will lose their entanglement density through disentanglement or chain scission to sustain the huge deformation³⁴. Just like the above said, we estimated that the dramatically strain would compulsorily

separate the MEH-PPV chains. But in the nano-scaled fibrils, the chains would force to be stretch in one direction which were perpendicular to the crazed direction and became straighten. This behavior could decrease the forming of structural defects and further increase the carriers' recombination. From both chain separation and chain straighten, the PL efficiency could be considerably increased after the forming of crazes.

Figure 9 shows the process of forming the crazes, if we assume that the volume of polymer is fixed, we can write

$$l_0 \times w \times d = l \times w \times d \times v_f$$

After rearranging we get

$$v_f = \frac{l_0}{l} = \frac{1}{\lambda}$$

where v_f means the volume fraction of fibrils in the craze, and λ is the extension ratio.

For crazes of PS (2M), we know that $\lambda_{\text{craze}}=400\%$, namely v_f equal to 0.25. Next, we try figure out the value of the volume fraction for crazed materials in the thin film (v_c). If the strain is denoted by ε , we could probably get v_c by

$$v_c = \frac{(\Delta l - 0.5\% \times l_0)wd}{l_0 wd} v_f = \frac{[l_0(\varepsilon - 0.5\%)]wd}{l_0 wd} v_f$$

and

$$v_c = (\varepsilon - 0.5\%) \times v_f = \frac{(\varepsilon - 0.5\%)}{\lambda}$$

where 0.5% is almost the maxima strain the non-crazed region could eached.

Under the same applied strain, the value of 0.5% has to be deducted. Then we assumed the intensity recorded by the photo-luminescence spectrophotometer could be written by

$$I = I_0 \times (1 - v_c) + I_c \times v_c$$

After rearranging, we get

$$\frac{I_c}{I_0} = \frac{I}{I_0} \times \frac{1}{v_c} - \frac{1 - v_c}{v_c}$$

where I is the intensity recorded by spectrophotometer at different degree of stretching, I_0 is the intensity of un-stretched sample and I_c is assumed to be the intensity contributed by the crazed region.

From the formula, it is clear that when crazes are not showed up, $I=I_0$. Figure 10 shows the diagram of I_c/I_0 versus ε for 0.1wt%, 0.5wt%, 1wt% blending samples which show intensity enhancement after stretching. At the beginning of stretching, we see that the value of I_c/I_0 is about 130 for 0.1wt% samples and decrease to about 20 with the continuous stretching. The other two samples also show the similar trend. These

mean that after the appearing of crazes, the intensity enhancement due to the crazed materials is at least about 20 times in magnitude of the original intensity. In addition, the amazing value of I_c/I_0 at the initial stage of stretching may be caused by the factor that the volume fraction of the craze tips which show the larger strain value¹⁵ than the other crazed regions and grow to midribs in the middle of crazes after the crazes were thickened is more than the latter period of the stretching process. To verify the arguments above, the 0.5wt% MEH-PPV/PS (2M+2k, with the same weight fraction) blending thin films were prepared. After stretching to $\epsilon=2\%$ (the blending thin film were too brittle to tolerate big strain), the same analytical methods were applied to this kinds of samples. The value of I_c/I_0 (about 165 ± 10) was larger than the cases which the molecular weight of PS matrix was pristine 2M. Yang had proposed that when the fraction of low molecular weight PS was increased comparing to the high molecular weight PS in PS blending thin film, not only the width of midrib, but also the value of λ_{craze} would increased with the fraction of low molecular PS¹⁵ which could be verify by the TEM observations. This statement exactly matched our experimental results, and that why the value of I_c/I_0 were huge in the beginning of stretching.

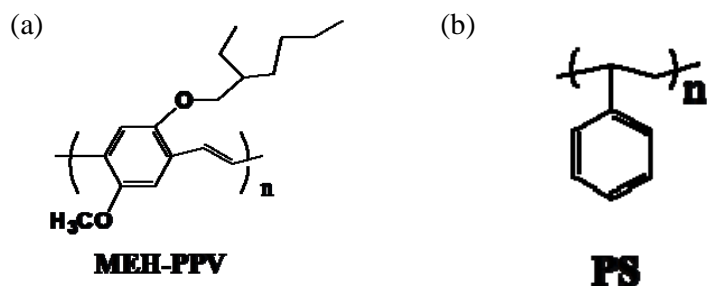


Fig. 7 The chemical structure of (a) MEH-PPV, (b) PS.

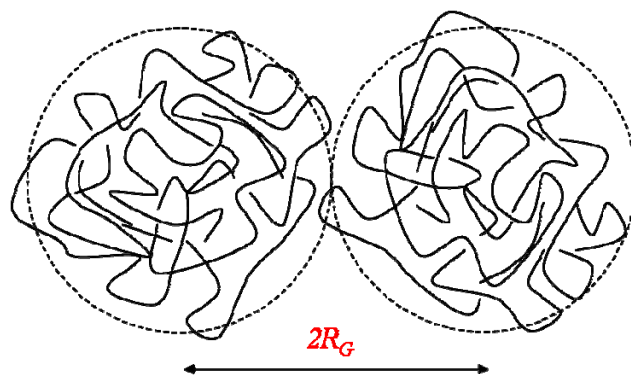


Fig. 8 The diagram of the spatial array of molecular coils under theta condition ($c=c^*$).

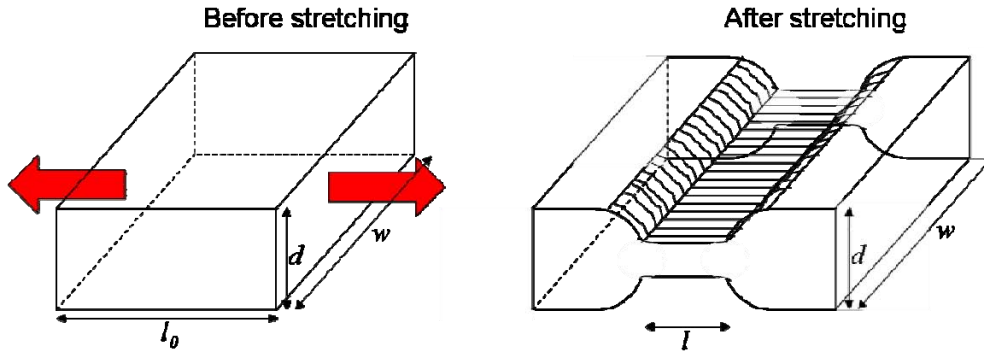


Fig. 9 The diagram of the process for forming crazes.

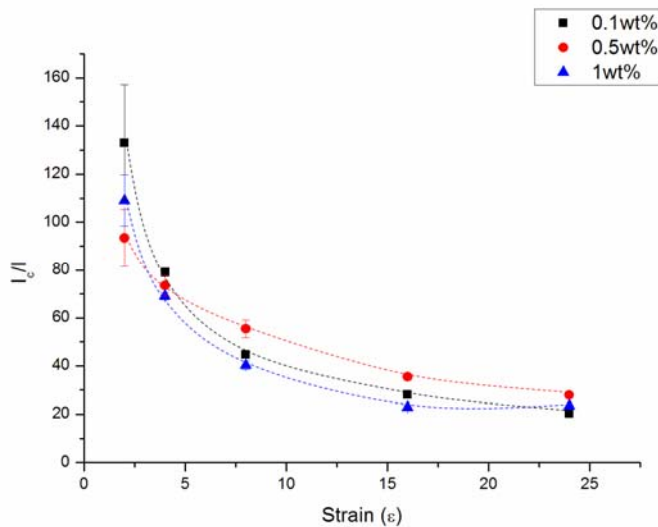


Fig. 10 The diagram of l/l_0 versus ϵ for 0.1wt%, 0.5wt%, 1wt% blending samples

Figure 11 shows the TEM micrographs of the samples which showed enhanced intensity after stretching. The structure of crazes these graphs expressed didn't make serious different with the normal pristine PS thin films. But for the high contents of MEH-PPV samples, e.g. 5wt% and 10wt% MEH-PPV/PS (2M), the situation was totally different, just like the Figure 13. There were aggregate-like substances appeared in these thin films, and obviously came from the excess additives of MEH-PPV. In the previously sections, we had reported that after stretching the thin films, the separation of conjugated chains and the following chains straighten would enhance the PL efficiency of conjugated polymers. For the 5wt% and 10wt% cases, the conjugated polymer chains had already aggregated even under the strain of 300% thus these conjugated polymer chains couldn't be separated and also had no chances to be straighten. These preliminary explanations could be applied to the interesting behaviors but still need further meticulous examination.

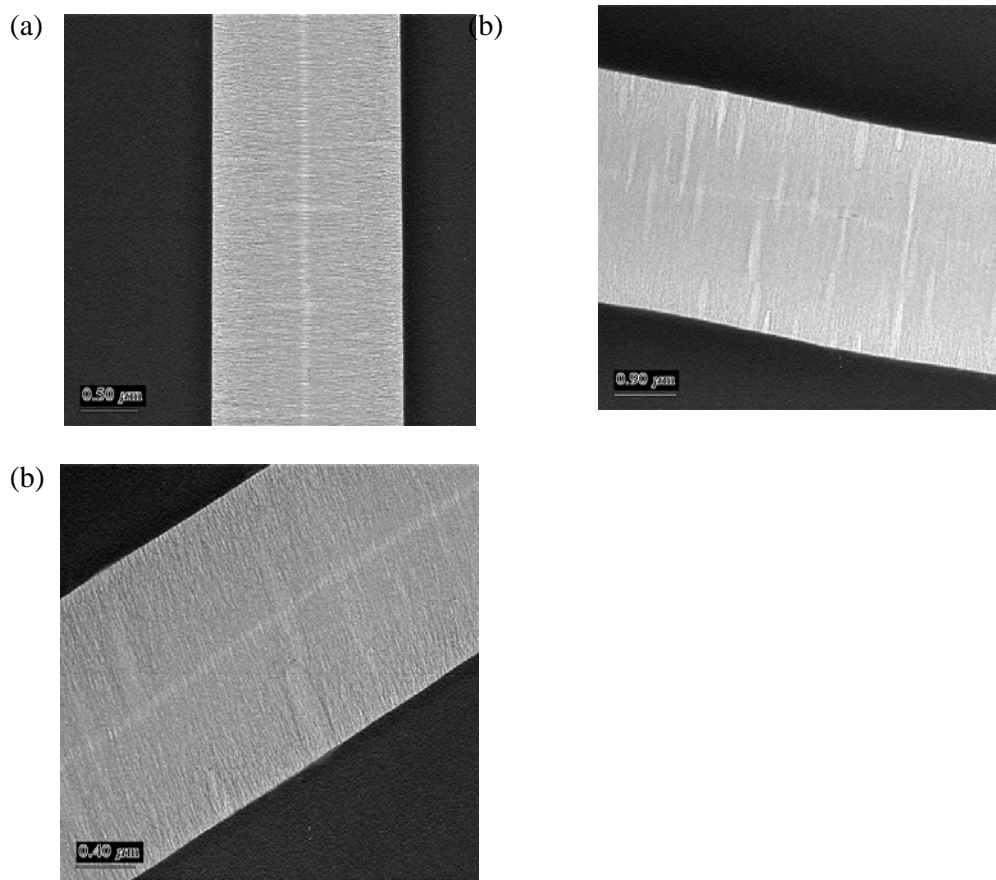


Fig. 11 The TEM micrographs of crazes for (a) 0.1wt% MEH-PPV/PS (2M), (b) 0.5wt% MEH-PPV/PS (2M), and (c) 1wt% MEH-PPV/PS (2M).

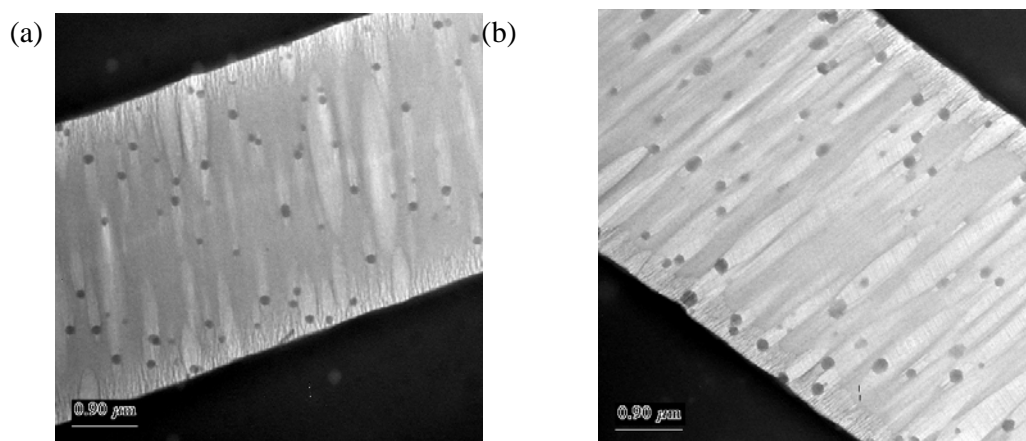


Fig. 12 The TEM micrographs of crazes for (a) 5wt% MEH-PPV/PS (2M), and (b) 10wt% MEH-PPV/PS (2M).

II-1.3 Conclusions:

In summary, by stretching the blending thin films of MEH-PPV/PS (2M) which showed the crazing behaviors, we could observe that the PL intensity was obviously enhanced in the low concentration of MEH-PPV situation, but not for the high concentration cases. The uniform deformation and SDZs had also been examined but the enhancement behaviors didn't show up. By further investigation, we estimate that when the conjugated polymer chains had been separated, e.g. the distance between the centers of conjugated polymer coils were larger than $2 R_G$, and the following chain straighten, the PL efficiency would increased. By the assumption of volume fraction for crazed materials, we also found that the PL intensity enhancement contributed to the appearing of crazes (I_c/I_0) was at least 20 times in magnitude to the intensity of un-strained thin film (larger than 130 times at most). All the observations showed that at some particular condition, the appearing of crazes would strongly affect the PL efficiency. These also indicated that the conformations of chains and the interaction between chains would strongly affect the luminescence behaviors of conjugated polymers. Different from the elder's research, our experiment confirmed this kind of viewpoint through the stretching test.

II-2 Single-molecule luminescence of conjugated polymers by solvent dewet

Traditional dewetting was performed at temperatures higher than T_g of polymer³⁵⁻³⁷. The thermal degradation of polymer chain may be serious at high temperatures especially for conjugated polymer. The previous work finished by our group have shown that photoluminescence intensity of MEH-PPV increased dramatically after thermal dewetting but the fact that high temperature may also broke down the conjugated structure in MEH-PPV causes an concern. Due to this, the exact enhancement factor may be much greater.

If we want to apply the photoluminescence enhancement in electroluminescence, the heat treatment has become another problem because high temperatures may change the properties of other parts of the device.

In light of this, "solvent dewet" performed at room temperature was attempted here where polymer chains gain tremendous increase of chain mobility in the solvent vapor⁴. Consequently, dewetting occurs because the energy barrier to achieve the equilibrium state is lowered compared to the polymer chains in dry solid films. Moreover, MEH-PPV/PS usually is difficult to undergo dewetting at 120 °C unless for very long annealing time. In contrast, solvent dewet occurs at room temperature, indicating that the solvent vapor has significantly lowered the energy barrier to the equilibrium state.

II-2.1 Experimental Procedures:

The MEH-PPV in this experiment was purchased from Sigma-Aldrich Chemical Co. with average number molecular weight $M_n = 150,000 \sim 250,000$ g/mol and molecular weight dispersity $M_w/M_n \sim 5$. The polystyrene was purchased from Pressure Chemical Co. with $M_w = 50,000$ g/mol with dispersity $M_w/M_n = 1.06$. Both polymers were used as received. The HPLC/SPECTRO toluene was purchased from TEDIA Co. To prepare the thin films, MEH-PPV/PS/toluene solution was firstly prepared. The ratio between MEH-PPV and PS was 25:75. The solution was stirred very slowly at 50 for 24 hours and filtered to remove impurities in solution. The polymer solution was then spin-casted on 1 cm x 1 cm silicon wafer. By changing the spin speed, we obtained different film thicknesses. In this experiment, the film thickness is about 20 nm. After spin-casting, the film was stored at ambient condition for 24 hours to evaporate the residual toluene in the film. During the sitting time, the samples were placed in a container packed with foil to prevent damages due to ambient light illuminations.

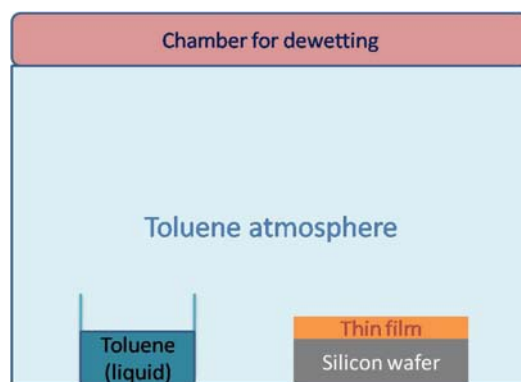


Figure 13 The schematic drawing of the chamber for solvent dewetting

The chamber for performing the “solvent dewetting” experiment was shown in Figure 13. The pressure in chamber was reduced to 20 mmHg and then toluene was injected into the container in chamber. The low pressure in the chamber forced the liquid toluene to evaporate quickly to reach its saturated state. The saturated vapor pressure of toluene at 25 °C is 28 mmHg. For dewetting experiments, the MEH-PPV/PS films were placed in the chamber for various periods of time and the corresponding extent of dewetting of each dewetting time was recorded by optical microscope or atomic force microscope. The solvent dewetting experiments were performed at room temperature.

Fluorescence spectrophotometer was used to measure the photoluminescence intensity of MEH-PPV/PS film before and after solvent dewetting. Different dewetting

time was adopted to control the extent of dewetting. We also used optical microscope and Atomic Force Microscope to characterize the topography of dewetted MEH-PPV/PS film. The scan mode of AFM in this experiment was Contact Mode with the septpoint was -2.0

For making the light emitting devices (LED) for studying the electroluminescence (EL), Poly(3,4-ethylenedioxythiophene) poly(styrenesulfonate), (PEDOT: PSS), was spin-coated on ITO glass to serve as the hole transport layer. The MEH-PPV/PS solution was then spin-coated on PEDOT. The film was solvent dewetted for 80 minutes and coated with TPBi and Al/LiF by thermal evaporation. ITO was used as the anode and Al/LiF the cathode for the EL device.

II-2 Results and Discussions:

II-2.1 Photoluminescence of dewetted MEH-PPV/PS film

The MEH-PPV/PS films subject to various dewetting times demonstrated different photoluminescence intensity and major peak position. In Figure 14, it shows that the PL intensity increased across the whole spectrum with dewetting time. With increasing dewetting time, the PL intensity increased up to several ten of times. At 540 nm, the PL intensity of 90-minute dewetted film is 47 times larger than the non-dewetted film.

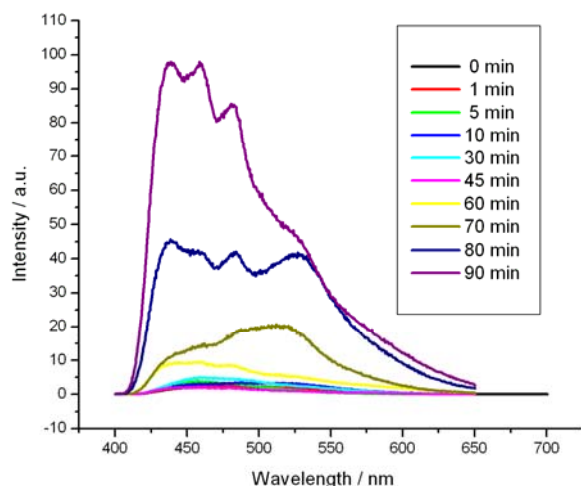


Fig. 14 PL spectra of MEH-PPV/PS film after different solvent dewetting time(the excitation wavelength is 350 nm)

It was readily observed that after 90-minute solvent dewetting, the most intensive emission peak of MEH-PPV/PS film has shifted to 440nm and there is 60 times PL enhancement at this wavelength. In addition to the blue shift of the major peak, it was also found that several minor and broad peak from 440~500nm became much more

intensive and sharper. After solvent dewetting, chain conformation must change and the new chain conformation is obviously more suitable for luminescence of conjugated polymer. Due to the blue shift of major peak of MEH-PPV/PS film, the conjugated length of MEH-PPV must have decreased. Thermal degradation of MEH-PPV was remarkably reduced since the dewetting experiment was performed at room temperature and as a consequence, it is reasoned that the blue shift and enhancement of PL was attributed to the much more constrained MEH-PPV chains.

II-2.2 Topography of dewetted MEH-PPV/PS film

For the 45-minute solvent dewetting sample (Figure 15c), the dewetting holes are visible, but rare, under an optical microscope. For the 60-minute dewetting sample (Figure 15d), the number of dewetting holes increased. In Figure 15e (70 minutes), the holes had become larger and clearer with their population increasing considerably. After 80-minute dewetting (Figure 15f), most of dewetting holes had contact with one another and the film evolved into a pattern of polyhedrons. For the 90-minute dewetting sample (Figure 15g), the original continuous film have converted into numerous fine droplets.

When using an AFM, better resolution and earlier detection of the hole formation was achieved in that for the 30-minute sample, there already exist many holes with high crest around them. The dependence of crest height versus hole depth is shown in Figure 17. On the 30-minute dewetting sample, the crest has become smooth as the holes became deeper. Nevertheless, only shallow holes (less than 4 nm) were observed in the samples of short dewetting times. For 45 minutes dewetting, the crest height increased slowly with increasing hole depth for hole depth less than the film thickness (20 nm) (Figure 18). It, however, increased much faster with increasing hole depth as the hole depth became greater than the film thickness, indicating the onset of sliding on substrate. For the 60-minute sample (Figure 19), the holes tend to have greater crest as compared to that in 45-minute sample of the same depth.

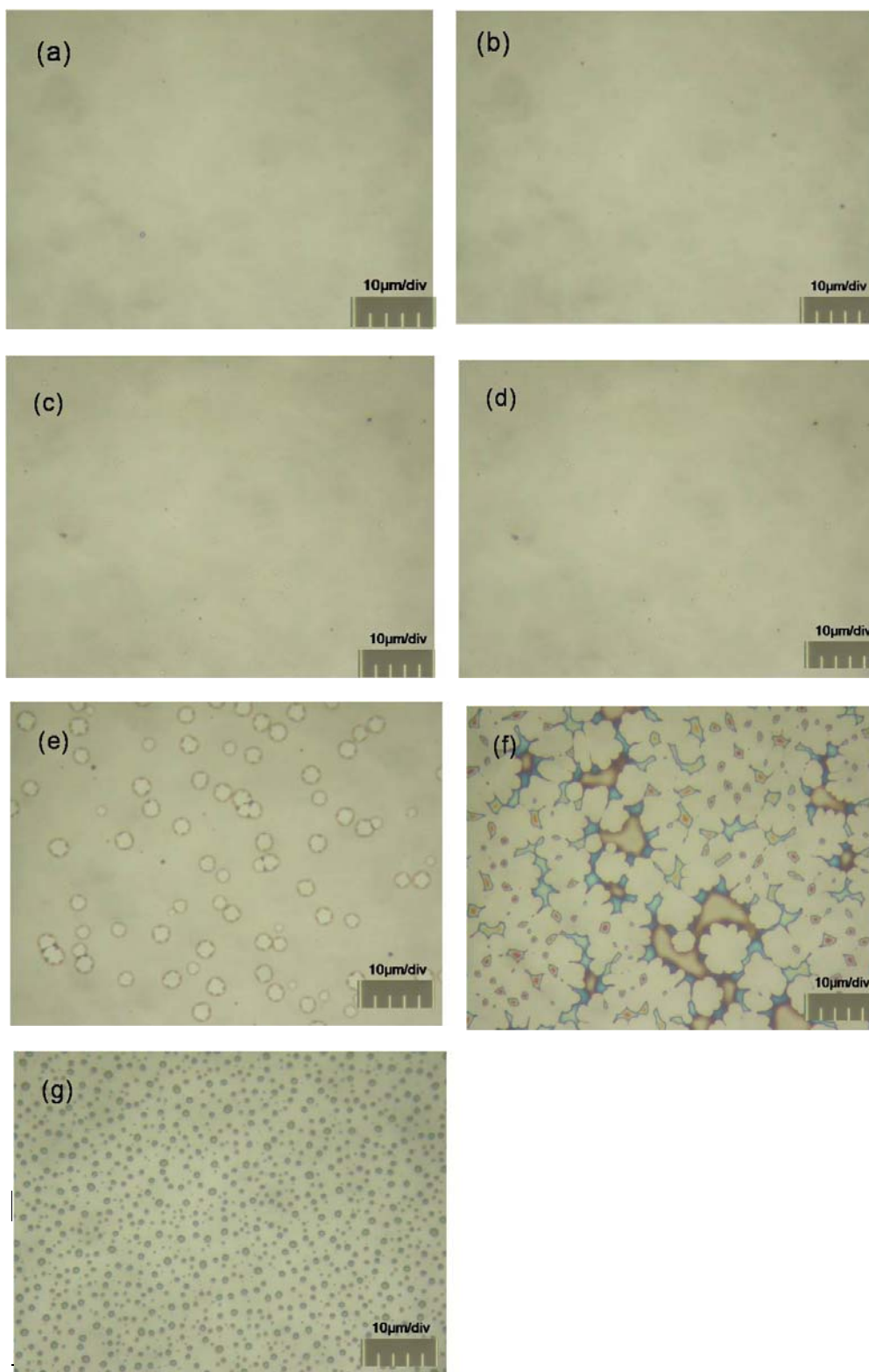


Fig. 15(a)~(g) Optical microscopy graph of MEH-PPV/PS film experiencing 0-minute, 30-minute, 45-minute, 60-minute, 70-minute, 80-minute and 90-minute solvent dewetting.

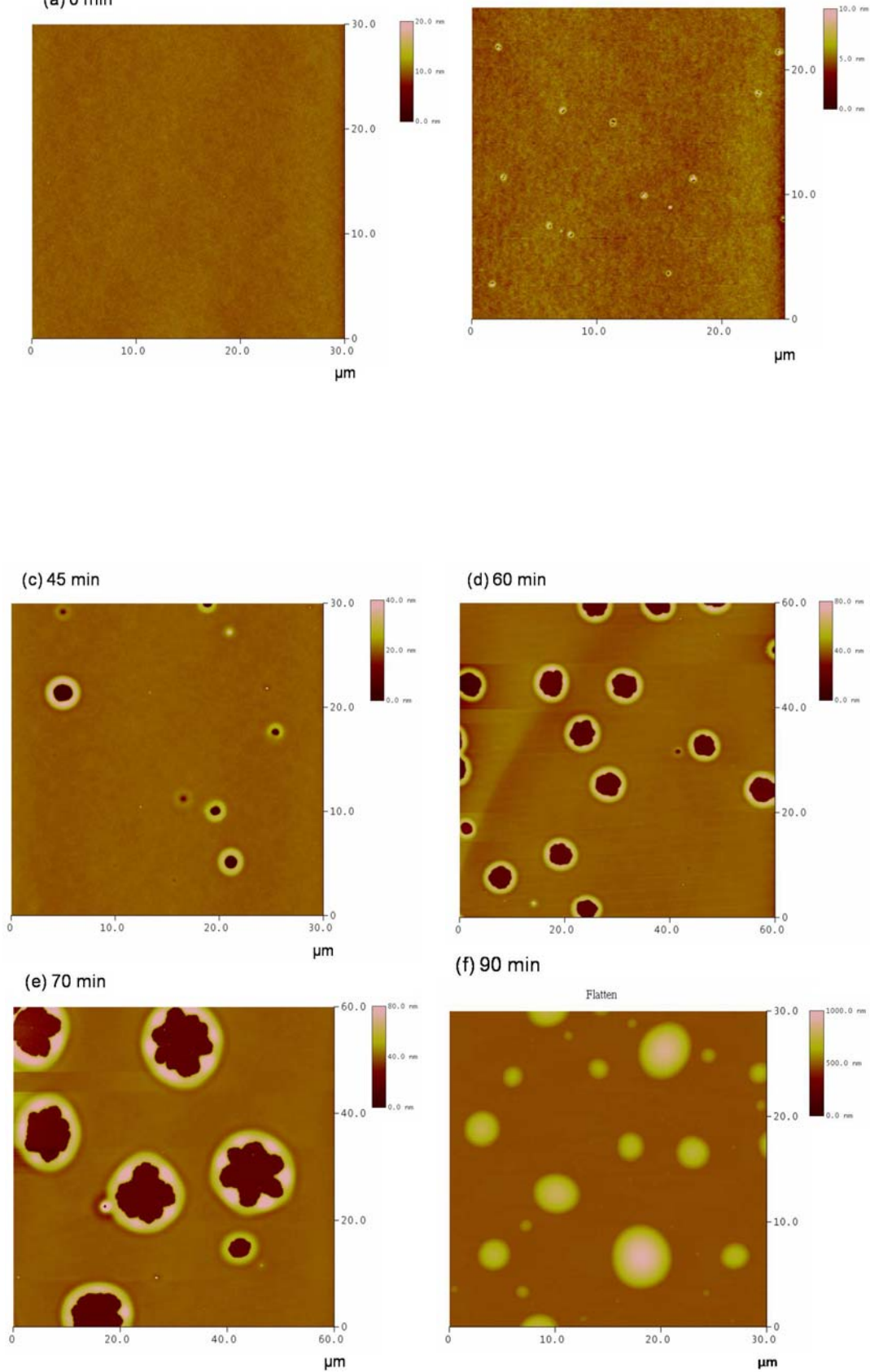


Fig. 16 (a)-(f) AFM image of MEH-PPV/PS film experiencing 0-minute, 30-minute, 45-minute, 60-minute, 70-minute and 90-minute solvent dewetting.

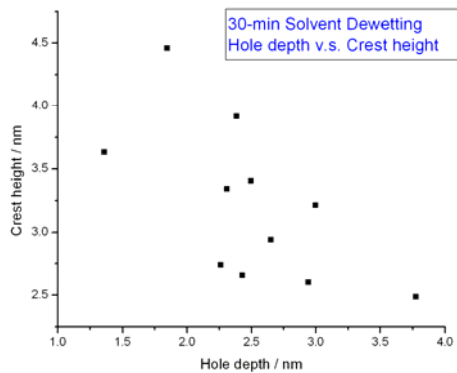


Fig. 17 Hole depth v.s. crest height distribution of 30-minute dewetting sample

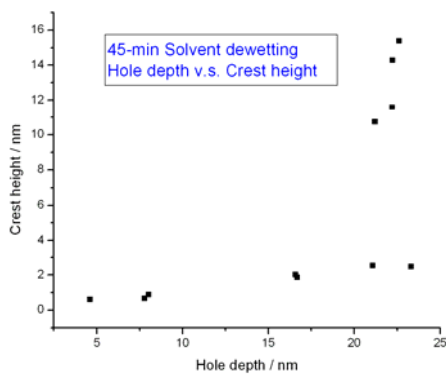


Fig. 18 Hole depth v.s. crest height distribution of 45-minute dewetting sample

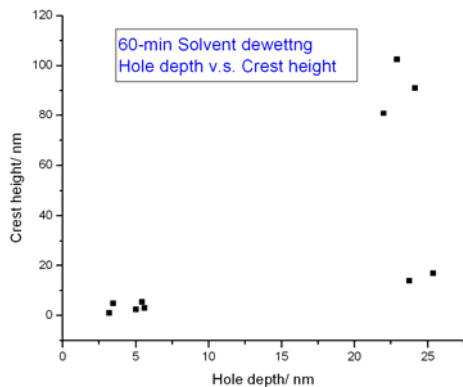


Fig. 19 Hole depth v.s. crest height distribution of 60-minute dewetting sample

II-2.3 Electroluminescence performance

Preliminary results were obtained in the electroluminescence study of the dewetted films. After the MEH-PPV/PS film had converted to fine droplets (80-minute)

(Figure 20), based on which an EL device was made. The schematic structure is shown in Figure 21. This device was capable to emit bright light (Figure 22). Further experimental exploration is still undergoing.

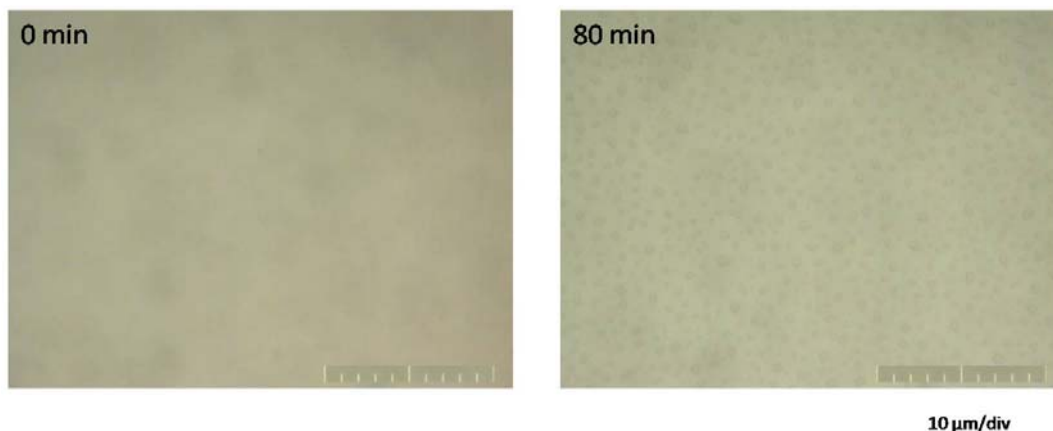


Fig. 20 MEH-PPV/PS droplets after solvent dewetting on PEDOT

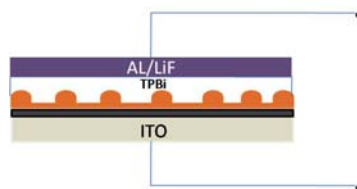


Figure. 21 Electroluminescence device structure

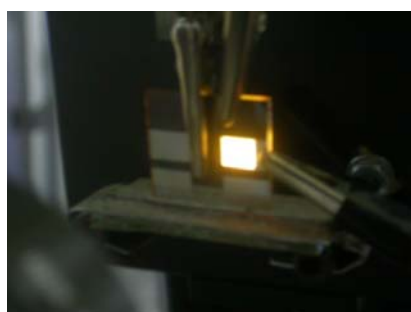


Figure 22. A PLED based on the solvent-annealed thin films.

II-3. Conclusions:

We have demonstrated successfully a novel dewetting method of solvent dewet. The dewetting holes by solvent dewetting have similar topography like that by traditional thermal dewetting. The PL enhancement after solvent dewetting was even larger than that after thermal dewetting. This solvent dewetting provides a non-destructive manner to dewet polymer film and has huge potential when dewetting

conjugated polymer in device.

References

1. Choi, D. H.; Cho, M. J.; Han, K. I.; Chang, I.-H.; Song, J. S.; Kim, J. H.; Paek, S.-H.; Choi, S.-H. *Synthetic Metals* 2006, 156, 685-689.
2. Cadby, A.; Dean, R.; Jones, R. A.; Lidzey, D. G. *Adv. Mater.* 2006, 18, 2713-2719.
3. Nguyen, T.-Q.; Martini, I. B.; Liu, J.; Schwartz, B. J. *J. Phys. Chem. B* 2000, 104, 237-255.
4. Schwartz, B. J. *Annu. Rev. Phys. Chem.* 2003, 54, 141-172.
5. Iyengar, N. A.; Harrison, B.; Duran, R. S.; Schanze, K. S.; Reynolds, J. R. *Macromolecules* 2003, 36, 8978-8985.
6. Moons, E. *J. Phys.: Condens. Mater* 2004, 14, 12235-12260.
7. Kim, T.-H.; Park, J. H.; Lee, T.-W.; Park, O. O. *Polymer* 2004, 45, 8567-8571.
8. Marletta, A.; Goncalves, V.; Balogh, D. T. *Brazilian Journal of Physics* 2004, 34, (2B), 697-698.
9. Kong, F.; Wu, X. L.; Yuan, R. K.; Yang, C. Z.; Siu, G. G.; Chu, P. K. *Journal of Vacuum Science & Technology A* 2006, 24, (2), 202-205.
10. He, G.; Li, Y.; Liu, J.; Yang, Y. *Appl. Phys. Lett.* 2002, 80, (22), 4247-4249.
11. Donald, A. M.; Kramer, E. J. *Polymer* 1982, 23, (3), 457-460.
12. Donald, A. M.; Chan, T.; Kramer, E. J. *Journal of Materials Science* 1981, 16, 669-675.
13. Yang, A. C.-M.; Kramer, E. J. *J. Polym. Sci., Polym. Phys. Ed.* 1985, 23, (7), 1353 - 1367.
14. Yang, A. C.-M.; Kramer, E. J.; Kuo, C. C.; Phoenix, S. L. *Macromolecules* 1986, 19, 2010-2019.
15. Yang, A. C.-M.; Kramer, E. J.; Kuo, C. C.; Phoenix, S. L. *Macromolecules* 1986, 19, 2020-2027.
16. Kramer, E. J.; Berger, L. L., Fundamental processes of craze growth and fracture. In *Advances in Polymer Science*, Springer Berlin / Heidelberg: 1990; Vol. 92, pp 1-68.
17. Kramer, E. J., Microscopic and molecular fundamentals of crazing. In *Advances in Polymer Science*, Springer Berlin / Heidelberg: 1983; Vol. 52-53, pp 1-56.
18. Sternstein, S. S.; Myers, F. A. *Journal of Macromolecular Science, Part B* 1973, 8, (3&4), 539 - 571.
19. Argon, A. S.; Hannoosh, J. G. *Philosophical Magazine* 1977, 36, (5), 1195-1216.
20. LeGrand, D. G.; Kambour, R. P.; Haaf, W. R. *Journal of Polymer Science: Polymer Physics Edition* 1972, 10, (8), 1195-1216.
21. Kitagawa, M. *Journal of Polymer Science: Polymer Physics Edition* 1976, 14,

- (11), 2095 - 2103.
22. Steger, T. R.; L. E. Nielsen. *Journal of Polymer Science: Polymer Physics Edition* 1978, 16, (4), 613-625.
 23. Brown, H. R. *Journal of Materials Science* 1979, 14, (1), 237-239.
 24. Farrar, N. R.; Kramer, E. J. *Polymer* 1981, 22, (5), 691-698.
 25. Wang, W.-C. V.; Kramer, E. J. *Journal of Materials Science* 1982, 17, (7), 2013-2026.
 26. Takahashi, K.; Hyodo, S. *Journal of Macromolecular Science, Part B* 1981, 19, (4), 695 - 713.
 27. Kawagoe, M.; Kitagawa, M. *Journal of Polymer Science: Polymer Physics Edition* 1981, 19, (9), 1423 - 1433.
 28. Yang, A. C.-M.; Wang, R. C.; Lin, J. H. *Polymer* 1996, 37, (25), 5751-5754.
 29. Yan, M.; Rothberg, L. J.; Kwock, E. W.; Miller, T. M. *Phys. Rev. Lett.* 1995, 75, (10), 1992-1995.
 30. Yang, A. C.-M.; Kunz, M. S.; Logan, J. A. *Macromolecules* 1993, 26, 1767-1773.
 31. Gettinger, C. L.; Hegger, A. J.; Drake, J. M.; Pine, D. J. *J. Chem. Phys* 1994, 101, (2), 1673-1678.
 32. Donald, A. M.; Kramer, E. J. *Journal of Materials Science* 1982, 17, 1871-1879.
 33. Meng, H.-F.; Hong, T.-M. *Phys. Rev. B* 2000, 61, (15), 9913-9916.
 34. Henkee, C. S.; Kramer, E. J. *Journal of Materials Science* 1986, 21, (1398-1404), 1398.
 35. Vrij, A. *Discuss. Faraday Soc.*, **42** 23 (1966)
 36. Cahn, J. w. *Chem, Phys.*, **42**, 93 (1965)
 37. Sferrazza, M.; Xiao, C.; Jones, R. A. L. *Phys. Rev. Lett.* **78**, 3693 (1997)

Chapter III

Nanoplastic Flows of Glassy Polymer Chains Interacting with Multiwalled Carbon Nanotubes in Nanocomposites

The nanocomposites based on well-dispersed carbon nanotubes (CNTs) embedded in carefully selected polymer matrices have increasingly attracted attention due to their great potentials for innovative mechanical, electrical, thermal, and optoelectronic properties. The outstanding advantageous properties of CNTs, such as the exceedingly high Young's modulus^{1,2} and conductivities^{3,4} and large flexibility limits and fracture strains,⁵ and the simple fact that they are tiny tubules with extremely high aspect ratios have made CNT an ideal filler for most polymers. In this context, the interactions between the embedded CNTs and the surrounding polymer chains not only are very interesting in the light of unveiling the fundamental chain behavior of the entangled macromolecules. They however also are of vital importance due to requirement of controllable CNT-polymer interactions down to the nanometer scales for successful modification of the physical properties. Previous work on CNTs as fillers in polymers has been focused primarily on the low-strain elastic behavior and cracking properties.⁶⁻¹⁵ Little attentions had been paid to the more important plastic flows regime that constitutes the major part of the mechanical performance before fracture. The elastic modulus and breaking stress in polystyrene (PS) were shown by Qian et al.^{9,16} to increase significantly by the addition of CNTs, pointing to the significant role of load transfer of CNTs. Watts et al.¹⁷ also identified the CNT pull-out mechanism during cracking, which effectively retarded the fracture in the CNTs-PS thin films. Apparently, observations of the CNT effects on stress transfer or failure processes strongly depend on the state of CNT dispersion and their interactions with the polymer chains.

Moreover, given the above-mentioned reinforcement effects, it is disappointing to observe that the optimal CNT reinforcement results were always observed in the

regime of a small CNT fractions ($\sim 1-2$ wt %)^{10,13,18-20} while the properties, like that

caused by most other fillers beyond a percolation threshold, fell off considerably for higher CNTs loadings (> 5 wt %).^{11,21} It indicates the necessity of more in-depth investigation of the CNT-polymer interactions over a wider range of deformation that includes both the elastic and plastic behavior. It is well-known that glassy polymers develop microscopic deformation zones of crazes²²⁻³⁵ or shear deformation zones

(SDZs)^{22,25,27,32} before fracture (Figure 1, parts a and b). The stress-induced local plastic flow that gives rise to the formation of these microscopic deformation zones

triggers extraordinarily large plastic strains ($\sim 200\text{-}300\%$) within the deformation

zones and is the basic molecular mechanism for yielding in most glassy polymers. The occurrence of crazes or SDZs depends on the entanglement density ν_e of the polymer matrix.^{22,30-32,34} In addition, crazing and shear yielding represent respectively the precursor of brittle and ductile fracture of glassy polymers. They are both produced by micronecking induced during the plastic flow,^{33-35,37,39} but the microstructures are quite different in that crazes are constructed by interconnected fibrils embedded in voids while SDZs are microscopically thinned smooth regions (Figure 1).^{22,25,28-32,34,36,39} The diameters of the craze fibrils are in the range of 6-20 nm, thus the local deformations are deemed to be nanoplastic flows. The microscopic reinforcement mechanisms of CNTs in glassy polymers should lie in the CNT interactions with these nanoplastic flows.

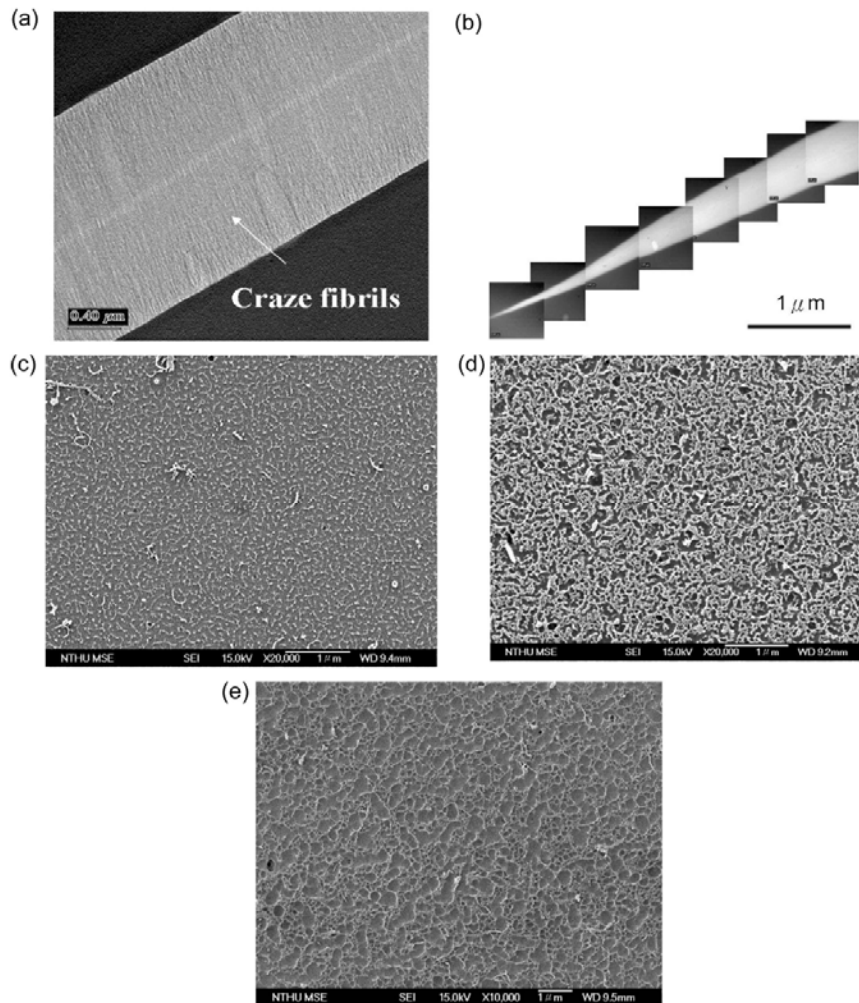


Figure 1. (a) a TEM micrograph of a craze in pristine PS film. (b) TEM micrograph of a shear deformation zone in pristine PPO film. (c-e) SEM micrographs of the plasma etched nanocomposites showing good CNT dispersion: (c) PS matrix with $c_0 = 2.0$ wt %; (d) PS matrix with $c_0 = 5.0$ wt %; (e) PPO matrix with $c_0 = 2.4$ wt %.

Previously, the role of multiwalled CNTs (MWCNTs) during crazing in PS-CNTs nanocomposites was explored^{38,39} and strain delocalization was identified to be the origin of fracture toughness enhancement. In these nanocomposites, most CNTs were observed to be excluded from crazes. In this study, more thorough investigation of the interactions between MWCNTs and polymer chains was undertaken by further examining the MWCNTs reinforcement in PS and in the SDZ-forming poly(phenylene oxide) (PPO). The work has led to a more complete and coherent scenario of the interactions between CNTs and polymer chains that satisfactorily explains reinforcement due to CNTs. The role of entanglement chain network during plastic flow in the nanocomposite was also unveiled, which sheds important light on the fundamental behavior of polymer chains in the glassy state.

III-1 Experimental Section

Monodisperse PS of molecular weight (M_w) 2000K (Pressure Chemical Co.) and PPO polymer with M_w 244K (Aldrich Chemical Co.) were used as-received. The MWCNTs (DESUN Nano Co., Taiwan) for this study, as determined from TEM examinations, have an average outer diameter around 10-35 nm and a length in the range of 10-30 μ m. The method of preparing the surface-grafted MWCNTs with long PS chains (PS- g -MWCNTs) was reported elsewhere^{38,39} and will not be re-emphasized here. The average molecular weight of the grafted PS in PS-MWCNTs was measured to be around 60K with polydispersity around 2.1 from gel permeation chromatography after the defunctionalization process.⁴⁰ As determined from thermogravimetric analysis (TGA), the weight fraction of PS in PS-MWCNTs nanocomposites is approximately 60 wt %. The average length of PS- g -MWCNTs is around 1-3 μ m.

The grafted MWCNTs were then mixed with the neat PS (or PPO) in toluene from which thin films (MWCNTs/PS or MWCNTs/PPO) with film thickness controlled at approximately 0.5 μ m were spincoated on clean glass slides from the solution. The fraction of the surface-grafted MWCNTs in the film (c_0) ranges from 0 to 10 wt %. The films were then transported and bonded to a supporting copper grid for mechanical experiments.^{30,31,34,38} Before the mechanical testing, aging at 120 °C for 1 h was routinely carried out for MWCNTs/PPO films to enhance the strain localization

required for growing SDZs.³⁶ During the mechanical test, the nanocomposite specimen was mounted in a strain jig, stretched under an optical microscope to observe the growth of deformation zones (crazes or SDZs).^{30,31,33–35,38} The samples were then examined under an AFM (Digital Instrumental, Nanoscope IIIa) for detailed analyses of the microdeformation, including calculations of the local stress and strain in the deformation zones.^{34,35} A transmission electron microscopy (TEM, JEOL JEM-2010) was used to obtain images of crazes or SDZs of the stretched samples. Taking advantage of the film-on-grid method,^{30,31,34,38} a large number of crazes and SDZs were examined, enabling the presentation here of typical and highly reproducible data for reliable interpretations. Widening of the microdeformation zones was monitored by using a video camera attached to an optical microscope and from the images of the growing crazes or SDZs the widening velocities were obtained. The dispersion of MWCNTs in the polymer matrix was examined by using a field-emission scanning electron microscope (FE-SEM; 4500) after gently etching the samples with oxygen plasma.^{38,39} The dispersion of MWCNTs has been excellent, as shown in Figure 1, parts c and d, such that the mechanical performance of the nanocomposites is consistent and reproducible.

III-2 Results and Discussions:

The plastic flow induced by local strains in glassy polymers gives rise to the formation of microdeformation zones. For brittle polymers such as PS, crazes arise from large local strains up to 300%, depending on the entanglement density.^{22,30–32} On the other hand, PPO, a model system for ductile glassy polymers, develops SDZ resulted from local strain around 100% upon application of stresses. According to Kramer’s ground-breaking work, the line of demarcation between the brittle and the ductile behaviors can be defined by a critical entanglement density v_e^c such that when $v_e > v_e^c$ (tight networks) shear deformation zones prevails, while crazes dominate in

the regime of $v_e < v_e^c$ (loose networks). Under ambient conditions, $v_e^c \sim 6 \times$

$10^{25}/m^3$.^{22,25,27} As will be shown later, the “tightness” of the chain entanglement networks determines not only whether the glassy polymer behaves in a ductile or brittle way, but also how the imbedded MWCNTs interact with the polymer chains during the plastic flow in the deformed glass.

III-2.1 Crazes Morphology.

In the pristine PS films, crazes initiated at approximation 1% strain (ϵ) and they

were generally straight, widening steadily as the strain increased, and the maximum width of creases could reach approximately $20\mu\text{m}$ (Figure 2a). Local fibril breakdowns within the crazes started at approximately $\varepsilon = 8\%$. Craze surface topography determined from AFM revealed that craze depth d increased almost linearly with craze width w when $w < w_c$ (see, for example, Figure 28 of ref 38). The critical width w_c is a

function of film thickness (for $0.5\mu\text{m}$ thick PS film, $w_c \sim 2.5\mu\text{m}$) and representing the

start of the microneck propagation.^{33–35,38,39} For $w > w_c$, craze depth became constant with w , indicating steady-state drawing of the crazing plastic flow. The films of the MWCNTs/PS composites with MWCNTs content (c_0) of 2 wt % demonstrated a quite different mechanical behavior in that the crazes were generally short and narrow (mostly less than $2\mu\text{m}$ wide) and no cracking was observed even at strains greater than 20% (Figure 2b). Moreover, although the craze depth d varied with craze width w following the same curve as that of pristine PS, w never reached w_c .^{38,39} It indicates that the micronecking characteristic of crazing was not altered by the presence of MWCNTs, however, the process was strongly suppressed. For films contain MWCNTs less than 1wt %, the observed effect due to MWCNTs on the microscopic deformation behavior was not obvious and no qualitative variations from that observed in films of $c_0 = 2$ wt % were noted.

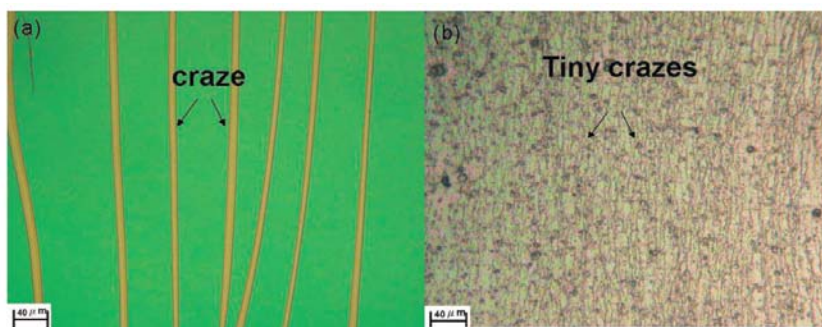


Figure 2. Optical micrographs of stretched (a) pristine PS films and (b) MWCNTs/PS composite film ($c_0 = 2$ wt %).

From AFM craze topography, the MWCNTs/PS nanocomposites evidently developed a concentrated plastic strain within the craze (Figure 3a, for $c_0 = 2$ wt%) with the maximum strain ε_p within the craze increasing with w but eventually leveling off for $w < 1 \mu\text{m}$. This is similar to the behavior of the pristine PS.^{33–35,38,39,41–43} Note that for narrow crazes ($w > 0.6 \mu\text{m}$), ε_p is just below 30%, a value very close to the reported elastic limit of carbon nanotubes.⁵ Figure 4a shows a TEM micrograph of a

craze tip propagating into a region of densely populated MWCNTs. The presence of the MWCNTs seems to have no effect on the growth of the craze in that the craze tip penetrates right through the MWCNTs. Since ε_p in the narrow crazes is below the elastic limit of MWCNTs, the MWCNTs within them thus can easily survive without inflicting breakage of the MWCNTs or being forced to substantially modify the plastic flow process.

In contrast, only in very rare incidence were intact MWCNTs observed within wider crazes. Generally, when craze width exceeds certain limit only broken pieces of MWCNTs were observed within the craze (Figure 4, parts b and c). Later examinations revealed that this width limit corresponds to that above which the local strain becomes significant in comparison to the extension limit of MWCNTs. The intact MWCNTs in the wider crazes were either incorporated from craze tips or from fibrillation of the “film” islands within crazes, which were formed by the merging of locally parallel crazes to trap intact MWCNTs within the new crazes. It seems quite unlikely for the plastic-flowed PS chains to pull MWCNTs across the craze boundaries into the microdeformation zones. Most MWCNTs embedded in the PS matrix appeared to stay outside the crazes. For those MWCNTs incorporated within crazes, depending on the drawing history, they were subject to different degree of stretching. Some were broken, leaving broken ends at the boundaries (Figure 4c). The local stresses within crazes in the films determined from AFM topography were in the order of 150 MPa. Since they were significantly less than the fracture stress of CNTs, the breakages of MWCNTs were likely to have occurred at the defect sites induced during surface treatments. Moreover, in the wider crazes ($w < 0.6 \mu\text{m}$) the plateau plastic strain ε_p (Figure 3a) had exceeded the flexibility limit of MWCNTs, hence either forced breakage or stress-shielding of the surrounding by the incorporated MWCNTs would occur. The latter should lead to a constraint craze widening, but it only played a minor role due to the insignificant number of MWCNTs within crazes.

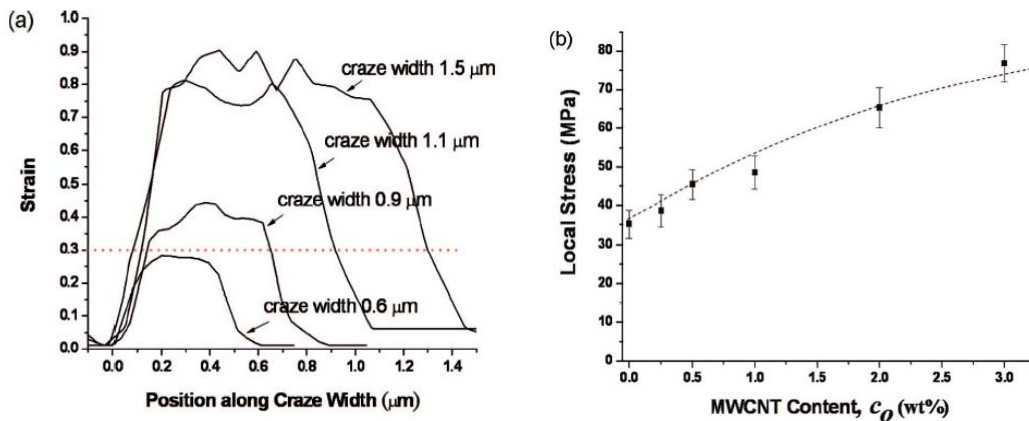


Figure 3. (a) Local strain distribution within a craze across the craze width for $c_0 = 2$ wt %, and (b) local stress within MWCNT/PS films with c_0 (for $w = 0.7\mu\text{m}$).

The exclusion of MWCNTs from crazing process was confirmed by AFM topography of the crazed films dry-etched by mild oxygen plasma,³⁸ of which protrusions arising from pileup of the slow-etched MWCNTs were observed bulging along the craze boundaries. The protrusion width, w_p , was determined by first measuring the apparent width of the protrusions as a function of etching time (inset of Figure 5a), and then the level-off value was taken as the protrusion width. The protrusion width was found to increase with craze width (Figure 5a). Correspondingly, the height of the protrusions was also found to increase with craze width, from 60 to 120 nm for w_p varying from 210 to 320 nm. This is consistent with the TEM observations (Figure 5b) that MWCNTs are excluded from crazes during fibrillation, engendering greater concentrations of MWCNTs at boundaries of the wider crazes.

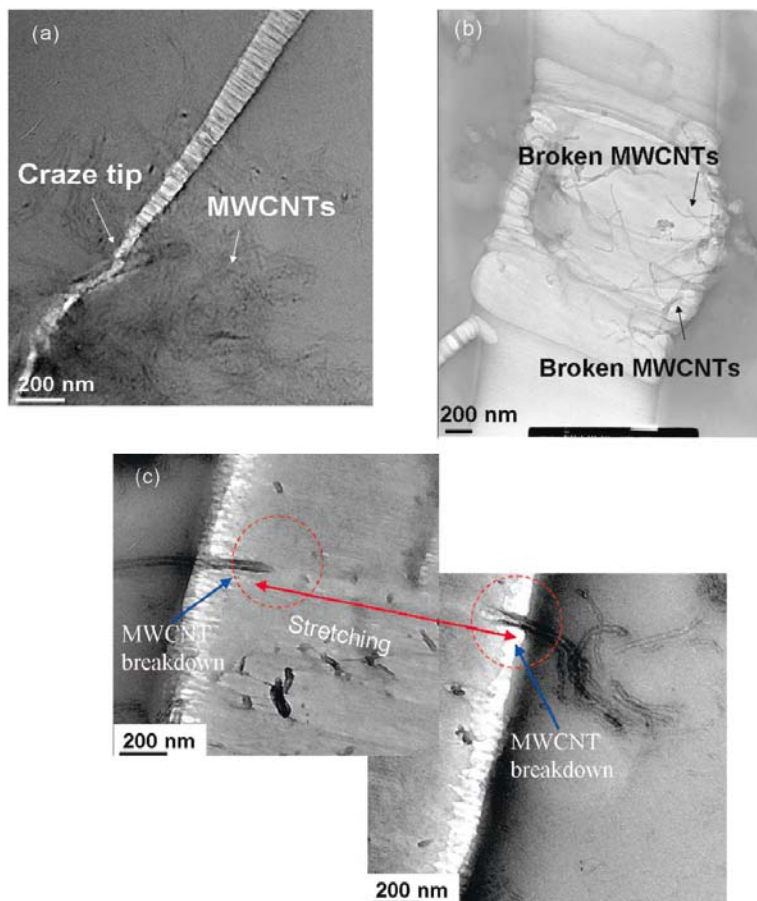


Figure 4. TEM micrographs of (a) a craze tip, (b) wider craze in MWCNT/PS films ($c_0 = 2 \text{ wt } \%$), and (c) fracture of nanotubes in MWCNT/PS films ($c_0 = 2 \text{ wt } \%$).

III-2.2 Fibrillation Modified by MWCNTs.

The local concentration of MWCNTs at craze boundaries was calculated, from the AFM data, to assess quantitatively how craze fibrillation was modified by the pileup of MWCNTs. Assuming all the MWCNTs in the course of craze widening would be excluded from crazes fibrillation, the local concentration of MWCNTs at craze boundaries (c_{pu}) can be readily shown to depend on the original concentration of MWCNTs (c_0) in the film, the craze width (w), protruding width (w_p), the film thickness at the craze (τ_c), mass density of craze ($\rho = 0.8 \text{ g/cm}^3$), and the original film thickness (τ_0), as

$$c_{pu} = c_0(1+w)\tau_c/2w_p\tau_0 \quad (1)$$

Obviously, eq 1 applies only for the regime where the wide crazes effectively exclude MWCNTs from the nanoplastic flow. Figure 5c indicates that c_{pu} increased approximately linearly with craze width w . The slope, increasing with c_0 , is quite steep. For a $2 \mu\text{m}$ wide craze, for example, c_{pu} goes up four times to $8 \text{ wt } \%$ in films of $c_0 = 2 \text{ wt } \%$. It indicated that the PS chains to be drawn across the craze boundaries need to pass through an increasingly denser network of MWCNTs at the boundaries. Thus, a greater drawing stress will be required for the PS chains to overcome the increasing chain frictions with the MWCNTs, and hence craze widening becomes more and more difficult. This ultimately enhances delocalization of the plastic flow of crazing.

The increase of chain friction due to MWCNTs was estimated using a Rouse tube model.⁴⁴ During the nanoplastic flow process of a glassy polymer, the chain pulled by the necking force f was assumed to undergo a constant sliding velocity v along the “topological tube” defined by the entangled chains, where f and v are related via the total frictional coefficient ζ_R of the whole chain, as

$$f = v \zeta_R \quad (2)$$

The pulling force f can be determined from the drawing stress σ during crazing and the cross-sectional area of the chain A_{chain} by $f = \sigma A_{chain}$. The cross-sectional area A_{chain} is approximately 0.688 nm^2 for a single PS chain in the tube where a total of 22 in average share the tube space.^{44,45}

For pristine PS films, the pulling force f was calculated to be $f \approx 0.065$ nN corresponding to the steady state necking stress $\tau \approx 94$ MPa determined from AFM results.^{34,35} The chain sliding velocity V was calculated from the craze widening speed, measured from video camera, at steady-state necking, which was then corrected by a factor of $N^{1/2}$ where N is the number of Kuhn monomer in the tube to take into account of the random coil chain conformation.^{44,46} For PS of $M_w = 2000K$, N is approximately 2800 (Kuhn monomer molar mass: 720 g/mol.). The craze widening velocity v was measured to be approximately 140 nm/s, the chain sliding velocity v thus is determined to be approximately 7400 nm/s. As shown in Figure 5d, v decreases slightly with craze widening until it levels as w passes the critical width w_c . The decrease obviously is due to strain hardening during the micronecking. From eq. 2, the friction coefficient of PS chain (ζ_{PS}) in the pristine polymer was calculated and found to be dependent on w . In the steady state necking regime, $\zeta_{PS} = 1.13 \times 10^{-5}$ kg/s was obtained (Figure 5e).

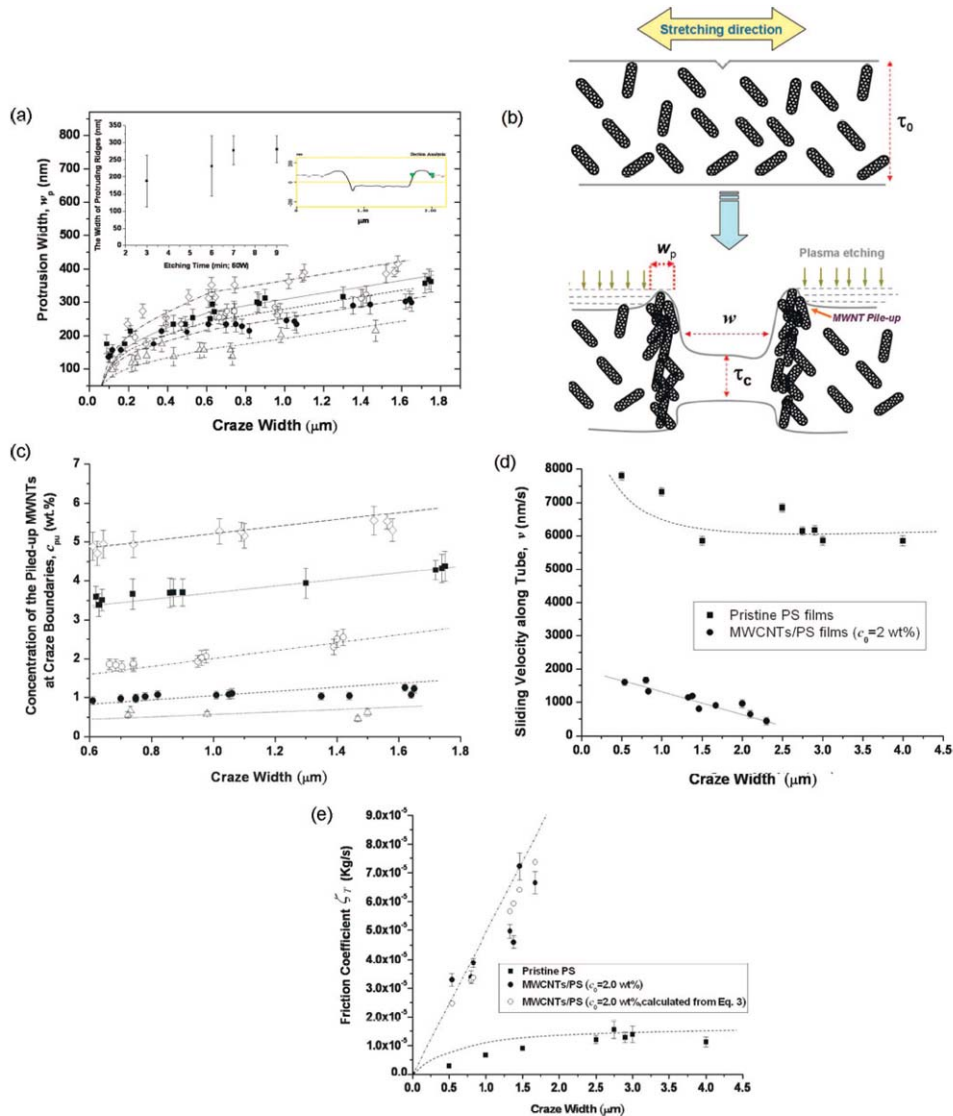


Figure 5. (a) Width of MWCNT pile-up at craze boundaries versus craze width, $c_0 = 3.0$ wt % ($c_0 = 2.0$ wt % ($c_0 = 1.0$ wt % ($c_0 = 0.5$ wt % ($c_0 = 0.25$ wt % . Insets: The width of the MWCNT pileup at the craze boundaries determined by AFM topographic profile and shown as a function of etching time, (b) a schematic of the MWCNT piled up at the craze boundaries, (c) the weight percentage of MWCNT protruding vs width of craze in MWNT/PS films, $c_0 = 3.0$ wt %; $c_0 = 2.0$ wt % ($c_0 = 1.0$ wt % ($c_0 = 0.5$ wt % ($c_0 = 0.25$ wt % , (d) tube sliding velocity of a PS chain versus craze width in pristine PS and MWCNT/PS films, and (e) the friction coefficient of a PS chain versus craze width in pristine PS and MWCNT/PS films.

For the MWCNT/PS films, MWCNT pileup at craze boundaries increases the chain frictional force during the nanoplastic flow. The friction coefficient ζ_T associated with a sliding chain going through a mixture of semidilute MWCNTs concentrations in PS where PS-CNT interactions dominate, can be described in terms of the number of nanotubes per volume v_{pu} and the MWCNT geometries (length l_{cnt} and diameter d_{cnt}) as

$$\zeta_T = \zeta_{PS} \left(1 + \frac{\pi (v_{pu} i_{cnt}^3)^3}{30\beta \ln\left(\frac{i_{cnt}}{d_{cnt}}\right)} \right) \quad (3)$$

where β is a numerical factor ($\beta = 1.32 \times 10^3$).^{47,48} This equation was originally developed⁴⁷ for the rheological behavior of CNTs/polymer nanocomposites by simulating the nanocomposite as one that contains rodlike particles in a matrix. Moreover, for the sake of simplicity, the chain conformation in the MWCNTs/PS systems is assumed to be approximately the same as that in pristine PS such that the length and molar mass of the Kuhn monomer remain unchanged. Using eq 3, the chain friction ζ_T during the nanoplastic flow can be calculated from c_{pu} , measured from AFM, and the nanotube geometrical constants ($l_{cnt} = 1.4 \mu\text{m}$, $d_{cnt} = 35 \text{ nm}$). As shown in Figure 5e, ζ_T increased almost linearly with craze width w for $0 < w < 2.0 \mu\text{m}$. Within the same craze width range, the chain sliding velocity v , readily obtained from ζ_T and the necking force f (from AFM stress analysis) using eq 2 (Figure 5d), was found to decrease steadily as craze widened, and for $w > 2.5 \mu\text{m}$, v became approximately zero, consistent with experimental observations that virtually all crazes in the MWCNTs/PS films were narrower than $2\mu\text{m}$. The chain friction during the nanoplastic flow can also be obtained directly from craze widening measured by video taping using eq 2. The frictional coefficient ζ_T so-obtained was found in excellent agreement with that determined based on MWCNT pileup (c_{pu}) at craze boundaries

(Figure 5e). This result strongly supports that the pileup of MWCNTs at craze boundaries caused an increase in chain friction, thus restricted the widening of existing crazes, forcing new craze initiation in the other regions to absorb the applied strain.

III-2.3 Embrittlement Induced by MWCNTs.

The exclusion of MWCNTs from the nanoplastic flow had increased the difficulty of chain fibrillation and forced a competition between initiation of new crazes and widening of the existing crazes, leading to a substantial reduction in craze widths. Since the probability of craze breakdown increases exponentially with craze width,^{30–32} delocalization of crazing reinforced the mechanical stability of the nanocomposite. Nevertheless, embrittlement ensued as the MWCNTs content increases to above 3 wt % (Figure 6). On the basis of the analyses above, the embrittlement was owing to the increased difficulty of craze initiation and the subsequent growth that follows the initiation. The local strain and stress within the incipient crazes, as shown in Figure 3, parts a and b, for $c_0 = 2$ wt %, increased with c_0 such that craze initiation would eventually be suppressed. When fewer crazes were available to absorb the deformation energy, cracking ultimately became preferentially favored.

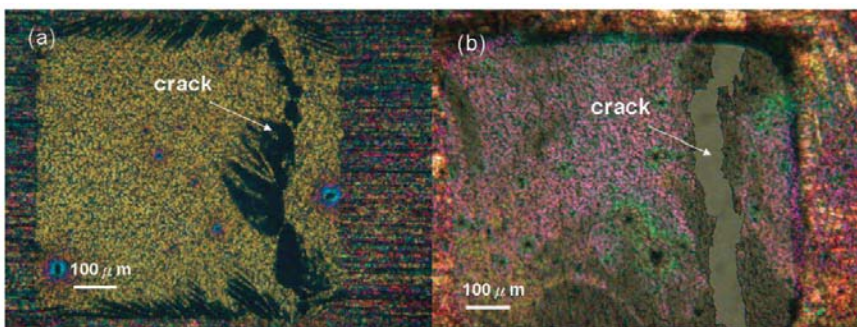


Figure 6. Optical micrographs of stretched MWCNT/PS films at high MWCNTs content: (a) 3 and (b) 5 wt %.

III-2.4 Straining of MWCNTs within SDZs.

With straight and sharp boundaries under an optical microscope, SDZs nucleated in the neat PPO films at approximately $\varepsilon=2\%$. They widened steadily as strain increased and eventually broke down to form cracks for $\varepsilon > 13\%$ (Figure 7a). Before voids were initiated, however, the SDZ could grow to a width as wide as $40\mu\text{m}$. The depth d of the SDZs, measured by AFM, followed a typical micronecking characteristic in that d increased linearly with w up to $w = w_c$, thereafter leveling to a constant depression (Figure 8a). The SDZs were generally smooth, under the TEM, with some secondary wavy striations lying perpendicular to the stretching direction.

The morphology of the SDZs underwent large changes when a small amount of

MWCNTs was added into the polymer matrix. For c_0 's as small as 1.5 wt %, the SDZs had become short and narrow ($w < 8 \mu\text{m}$), more numerous, and the film remained

intact for ε 's up to $\sim 16\%$ (Figure 7b). These effects are quite similar to that observed

in MWCNTs/PS systems where strain delocalization had modified the nanoplastic flow behavior. However, these SDZs manifested very different interactions with the embedded MWCNTs, as compared to crazes, in that the MWCNTs were found to draw into the SDZs regardless of the zone width, as revealed under TEM (Figure 7, parts c and d). The incorporated MWCNTs were either perfectly straightened along the drawing direction (for smaller diameters, ca. $> 20 \text{ nm}$, Figure 7c), or aligned to a lesser degree but with obvious local debonding taking place at the interfaces with the polymer matrix (for these MWCNTs of greater diameters, Figures 7d). Clearly, there is no pileup of MWCNTs at the boundaries of the deformation zones. Consistent with this observation, the AFM topography of the mildly etched SDZ also did not show any protrusions at the zone edges (Figure 8b). It is thus obvious that the MWCNTs can be drawn by the nanoplastic flow into the SDZs.

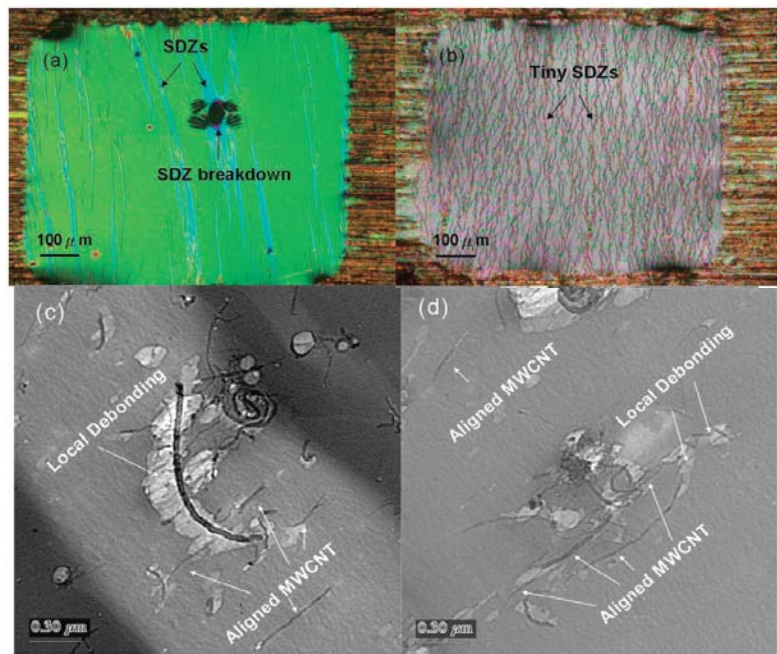


Figure 7. Optical micrographs of stretched (a) pristine PPO films, (b) MWCNTs/PPO composite film (weight fraction of MWCNT is 1.5 wt %), and (c) TEM micrographs of narrow SDZ, and (d) TEM micrograph of a wider SDZ in MWCNT/PPO films ($c_0 = 1.5$ wt %).

The incorporation of the MWCNTs in the nanoplastic flow, furthermore, produced an accelerated strain hardening of the flow in that the leveling depression ds decreased as c_0 increased (Figure 8, parts a and e). It decreased from 0.26, of the original thickness for the neat resin, to 0.13, for $c_0 = 2.4$ wt % (Figure 8a). Since the draw ratio

(λ_{SDZ}) in the SDZs scales very closely with the leveling depression ds via $\lambda_{SDZ} \sim \tau_0/(\tau_0 - 2ds)$,

^{22-25,27,30-32} The decrease of (ds/τ_0) from 0.26 to 0.13 for a change from $c_0 = 0$ to $c_0 = 2.4\%$ translates into a decrease of λ_{SDZ} from 2.08 to 1.35, a 3-fold decrease of the molecular strain. This, however, is consistent with the fact that the volume fractions of MWCNTs (c_0 's) are already significantly greater than the percolation threshold of MWCNTs, approximately 0.08 vol %, for the MWCNTs. The slope of the linear increase of d versus w during the initial necking also decreases with c_0 , indicating an increase of chain friction in the PPO/MWCNTs nanocomposites.

The increase of chain friction of the nanoplastic flow in MWCNTs/PPO was estimated by use of the Rouse chains model as applied for crazes in the PS systems before with A_{chain} of the PPO chain approximately 0.55 nm^2 . For both the pristine PPO and MWCNTs/PPO films, the tube sliding velocities v 's, measured from SDZ widening, were shown, with somewhat large data fluctuations, to be indistinguishable from each

other; they were almost constant ($\sim 1500 \text{ nm/s}$) but in fact slowly decrease with w

(Figure 8c). The friction coefficient ζ_T was found to increase with the w when $w < w_c$ but then began leveling-off for $w > w_c$ (Figure 8d). The addition of the MWCNTs

(1.5wt.%) in PPO had raised the chain friction from $\zeta_{PPO} \sim 4.3 \times 10^{-5} \text{ kg/s}$ to $\zeta_T \sim 7.5$

$\times 10^{-5}$ kg/s, but the overall trend remains unchanged. Clearly, the incorporation of MWCNTs during the nanoplastic flow had dramatically reduced the extensibility of the entanglement network of the PPO matrix.

III-2.5 Strain-Hardening of the Entangled Chains.

The intriguing differences between SDZs and crazes in the interactions with MWCNTs obviously should be related to the plastic flow properties of the entanglement network incurred during the local deformation. According to Kramer,^{22–25,27,30–32} the state of deformation induced by the deformation zones is related to the structure of entanglement network. For example, the average draw ratio of the plastic flow, λ_{craze} or λ_{SDZ} , scales approximately with the extensibility of the chain network, λ_{max} , defined as $\lambda_{\text{max}} = l_e/d_e$ where l_e is the contour length between entanglements and d_e is the direct distance between them.^{22–25,27,30–32} The PPO is known to have a tighter entanglement chain network ($\lambda_{\text{max}} = 3.1$, $v_e = 1.5 \times 10^{26}$ chains/m³) compared to that of PS ($\lambda_{\text{max}} = 4.2$, $v_e = 3.3 \times 10^{25}$ chains/m³) (shown schematically in Figure 9a).^{22,32} Furthermore, the deformations of the entanglement networks in both PS and PPO had been explored before by microscopic stress analyses from the AFM topography.^{33–35,37–39}

It was found that both entanglement networks manifested a twostage process, strain-softening and strain-hardening, during the deformation with a critical strain ε_h (dubbed as the hardening strain) dividing these two regimes.^{34,37} The hardening strains ε_h 's for crazing in the loose chain network of PS and that for SDZs in the tighter PPO chain network were quite different. The hardening strain ε_h of PS (of molar mass 2M) was determined to be $\varepsilon_h = 1.4$ while it was approximately $\varepsilon_h = 0.3$ for PPO.³⁴

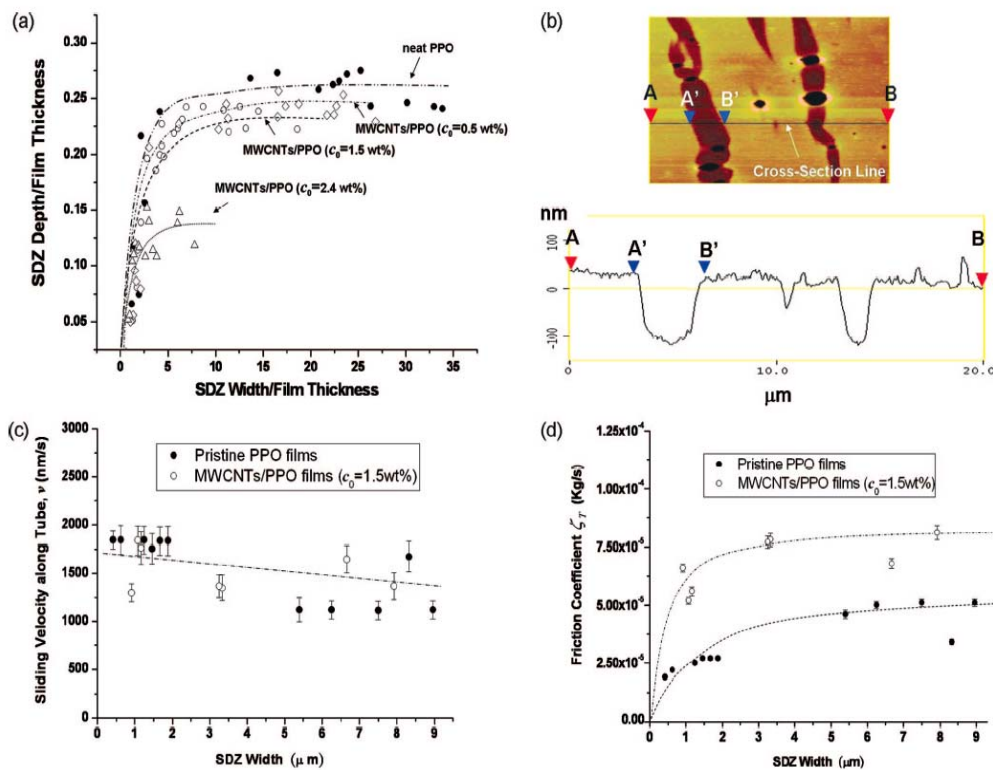


Figure 8. (a) SDZ depth vs SDZ width in the pristine PPO and MWNTs/PPO films: pristine PPO films ($c_0 = 0$ wt %) (ζ , $c_0 = 2.4$ wt %) (ζ , $c_0 = 1.5$ wt %) (ζ ; $c_0 = 0.5$ wt %) (ζ). (b) AFM micrographs of the stretched and etched MWNTs/PPO films. (c) Tube sliding velocity of a PPO chain versus SDZ width in pristine PPO and MWCNT/PPO films, (d) Friction coefficient of a PPO chain versus SDZ width in pristine PPO and MWCNT/PPO films. (e) Normalized SDZ depth versus c_0 .

With this, the drawing mechanics of the plastic flows were further analyzed by comparing ε_h 's of the two polymers with the corresponding maximum strain ε_p 's (the plateau strain) in the films (Figure 9b). Although the plateau strains ε_p 's for both PS and PPO increase monotonically with w , the plateau strains ε_p 's for $w < 5 \mu\text{m}$ in MWCNTs/PS were smaller than the hardening strain ($\varepsilon = 1.4$) of the PS chain network. Recalling that virtually all the crazes formed in the MWCNTs/PS films were thinner than $2 \mu\text{m}$ in width, it indicates that the PS chains in the nanoplastic flows were still in the strain-softening stage, incapable of drawing the relatively much more rigid MWCNTs into crazes. On the contrary, the plateau strains ε_p 's in the SDZs of MWCNTs/PPO would be greater than ε_h of the PPO chain network ($\varepsilon = 0.3$) for $w > 0.6 \mu\text{m}$. Since most SDZs in the MWCNTs/PPO nanocomposite were wider than that ($0.6 \mu\text{m}$), the PPO chains in the nanoplastic flow were able to pull the MWCNTs into the local deformation zones.

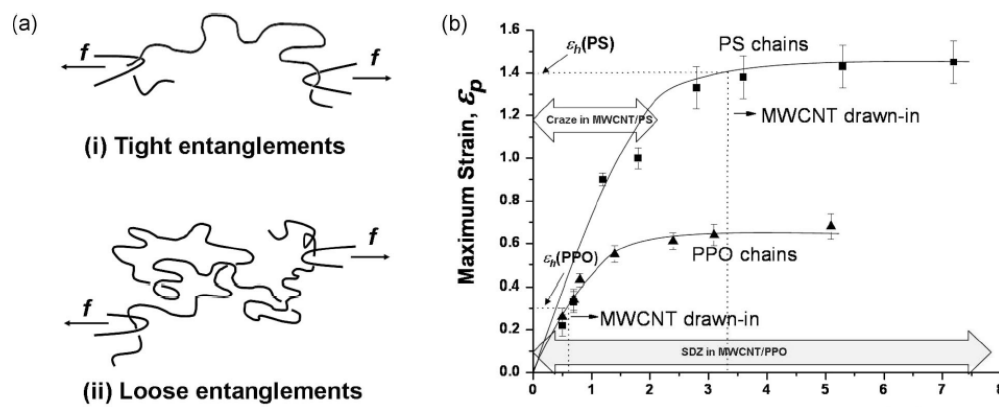


Figure 9. (a) Schematic drawings of tight and loose chain entanglements, and (b) the local maximum strain versus the width of local deformation zones.

III-3 Discussions

The length scales of interactions during the drawing of surface grafted MWCNTs by the nanoplastic flows of glassy polymers may be in the order of tens of nanometers, as hinted by the diameter of MWCNTs (~25 nm), due to the fact that some degrees of local bending of the MWCNTs obviously deemed inevitable. Since the bending moment of CNTs increases approximately to the third power of the tube diameter, drawing of CNTs would become more dominant, as opposed to polymer draining through the CNTs, during the nanoplastic flows when the diameter of the CNTs decreases. Early results seem to confirm this picture in that single-walled CNTs (SWCNTs) were observed being drawn into crazes in films of the bulky polybenzoxazoles macromolecules where SWCNTs were surface treated by a physical adsorption means.⁴⁹

In the light of this, other than the improved compatibility that has led to uniform dispersion of CNTs in the polymer matrix, the effects of molecular weight and the amount of the grafted polymers⁵⁰ may be primarily on the magnitude of tube friction ζ_{τ} during the nanoplastic flows. Higher molecular weights and greater polymer fractions are expected to increase the frictions. It, however, would not qualitatively alter the major observations obtained in this experiment. Further explorations in this direction is interesting but is beyond the scope of this study.

The range of CNT fractions (0-10 wt %) explored in this experiment covers the regime (>0.1 wt %) where the dispersed CNTs percolate electrically.⁴⁹ However, electric percolation does not correspond to mechanical percolation where the CNTs would effectively form a network that is fully stress-bearing. As revealed by the PS systems, CNT displacement that causes substantial modifications of the purported CNTs network occurs upon stretching as polymer chains draining through the CNTs to cause local CNT pileup at the craze boundaries. In the strainhardening system of PPO, although the CNTs can be drawn into the SDZs, they at the same time did not escape the fate of strain localization and underwent fracture at a strain not significantly greater

than those without them. Apparently, control over the state of entanglement between CNTs and stability of the CNTs network requires further material engineering that exploits the properties and geometries of individual CNTs as well as nanostructuring them into right space. The notion of a stress-bearing entanglement network of CNTs that effectively shield the polymer composite from mechanical stress remains to be tested by further experiments and is out of the scope of the intended study here. For the range of very dilute CNT fractions (>1 wt %), the effect on the nanoplastic flow is minute, however.

With the micromechanical analyses based on AFM data, the interactions between the embedded MWCNTs and the glassy polymer chains during the nanoplastic flows can be understood in a simple and coherent framework in terms of the plastic flows micromechanics and the properties/structure of the chain entanglement network. The complicated effects of filler arising from MWCNTs in glassy polymers can be understood further by pursuits using this approach. The important fundamental behavior of glassy polymer chain during the nanoplastic flows of crazing or shear yielding can be unveiled with advances of the chain-MWCNTs interactions.

III-4 Conclusions

In conclusion, the surface-grafted MWCNTs dispersed in a polymer matrix dramatically toughen the glassy polymer by delocalization of plastic flows, engendered by a significant increase of chain friction during microdeformation. The interactions between the MWCNTs and polymer chains, however, are quite different for craze-forming brittle polymer (PS) and SDZ-forming ductile polymer (PPO), which can be attributed to variations in the chain entanglement network structure. For PS, the CNTs-polymer interactions during the plastic flow is in the regime of polymer strain softening in which the polymer chains drawn into crazes are filtering through the pileup of MWCNTs at craze boundaries. The pileup is resulted from the incapability of the softened chains to pull the rigid CNTs into the nanoplastic flow. In this situation, chain friction increases linearly with craze width during widening of the craze and ultimately forces nucleation of new crazes, leading to delocalization of the strain. In contrast, the PPO chains undergo strain-hardening during the nanoplastic flow and are capable to draw MWCNTs into the SDZs, leaving no pileup of MWCNTs at the zone boundaries. The delocalization effect due to MWCNTs is thus much smaller as compared to that in MWCNTs/PS and the SDZs can still grow to a width significantly wider than crazes in PS/MWCNTs of the same MWCNTs loadings. The physical participation of MWCNTs in the nanoplastic flows of PPO has generated an increase of chain friction although it does not alter qualitatively the dependence of chain friction on the degree of drawing during the flow. The incorporation of MWCNTs in

the flow considerably reduce the extensibility of the glassy polymer, giving rise to substantially lower plateau strain of the plastic flow (3 time reduction for $c_0 = 2.4$ wt %) and higher draw stress (1.5 time increase for $c_0 = 2.4$ wt %). At high MWCNTs contents in either PS or PPO, the increase of chain friction eventually suppresses the formation of crazes or SDZs and ultimately leads to embrittlement of the nanocomposites.

References and Notes

- (1) Yu, M. F.; Lourie, O.; Dyer, M. J.; Moloni, K.; Kelly, T. F.; Ruoff, R. S. *Science* **2000**, *287*, 637.
- (2) Hwang, G. L.; Hwang, K. C. *Nano Lett.* **2001**, *1*, 435.
- (3) Bekyarova, E.; Itkis, M. E.; Cabrera, N.; Zhao, B.; Yu, A.; Gao, J.; Haddon, R. C. *J. Am. Chem. Soc.* **2005**, *127*, 5990.
- (4) Hecht, D.; Hu, L.; Gruner, G. *Appl. Phys. Lett.* **2006**, *89*, 133112.
- (5) Yakobson, B. I.; Campbell, M. P.; Brabec, C. J.; Bernholc, J. *Comput. Mater. Sci.* **1997**, *8*, 341.
- (6) Yang, Y.; Gupta, M. C.; Dudley, K. L.; Lawrence, R. W. *Nano Lett.* **2001**, *5*, 2131.
- (7) Hill, D. E.; Lin, Y.; Rao, A. M.; Allard, L. F.; Sun, Y. P. *Macromol.* **2002**, *35*, 9466.
- (8) Liu, C. H.; Fan, S. S. *Appl. Phys. Lett.* **2005**, *86*, 123106–1.
- (9) Qian, D.; Dickey, E. C. *Appl. Phys. Lett.* **2000**, *76*, 2868.
- (10) Blond, D.; Barron, V.; Ruether, M.; Ryan, K. P.; Nicolosi, V.; Blau, W. J.; Coleman, J. N. *Adv. Funct. Mater.* **2006**, *16*, 1608.
- (11) Hwang, G. L.; Shieh, Y. T.; Hwang, K. C. *Adv. Funct. Mater.* **2004**, *14*, 487.
- (12) Coleman, J. N.; Cadek, M.; Blake, R.; Nicolosi, V.; Ryan, K. P.; Belton, C.; Fonseca, A.; Nagy, J. B.; Gun'ko, Y. K.; Blau, W. J. *Adv. Funct. Mater.* **2004**, *14*, 791.
- (13) Singh, S.; Pei, Y.; Miller, R.; Sundararajan, P. R. *Adv. Funct. Mater.* **2003**, *13*, 868.
- (14) Zhu, J.; Kim, J.; Peng, H.; Margrave, J. L.; Khabashesku, V. N.; Barrera, E. V. *Nano Lett.* **2003**, *3*, 1107.
- (15) Li, X.; Gao, H.; Scrivens, W. A.; Fei, D.; Xu, Xiaoyou; Sutton, M. A.; Reynolds, A. P.; Myrick, M. L. *Nanotech* **2004**, *15*, 1416.
- (16) Qian, D.; Dickey, E. C. *J. Micro.* **2001**, *204*, 39.
- (17) Watts, P. C. P.; Hsu, W. K. *Nanotech* **2003**, *14*, L7.
- (18) Liu, T. X.; Phang, I. Y.; Shen, L.; Chow, S. Y.; Zhang, W. D. *Macromolecules* **2004**, *37*, 7214.
- (19) Zhang, W. D.; Shen, L.; Phang, I. Y.; Liu, T. X. *Macromolecules* **2004**, *37*, 256.

- (20) Machado, M. A.; Valetini, L.; Biagiotti, J.; Kenny, J. M. *Carbon* **2005**, *43*, 1499.
- (21) Meincke, O.; Kaempfer, D.; Weickmann, H.; Friedrich, C.; Vathauer, M.; Warth, H. *Polymer* **2004**, *45*, 739.
- (22) Kramer, E. J. *AdV. Polym. Sci.* **1983**, *52/53*, 1.
- (23) Donald, A. M.; Kramer, E. J. *J. Polym. Sci.: Polym. Phys.* **1982**, *20*, 899.
- (24) Donald, A. M.; Kramer, E. J. *J. Polym. Sci.: Polym. Phys.* **1982**, *23*, 1183.
- (25) Donald, A. M.; Kramer, E. J. *Polymer* **1982**, *23*, 461.
- (26) Donald, A. M.; Kramer, E. J. *Polymer* **1982**, *23*, 457.
- (27) Henkee, C. S.; Kramer, E. J. *J. Polym. Sci.: Polym. Phys.* **1985**, *22*, 721.
- (28) Yang, A. C.-M.; Kramer, E. J. *J. Polym. Sci.: Polym. Phys.* **1985**, *23*, 1353.
- (29) Yang, A. C.-M.; Kramer, E. J. *J. Mater. Sci.* **1986**, *21*, 3601.
- (30) Yang, A. C. M.; Kramer, E. J.; Kuo, C. C.; Phoenix, S. L. *Macromolecules* **1986**, *19*, 2010.
- (31) Yang, A. C. M.; Kramer, E. J.; Kuo, C. C.; Phoenix, S. L. *Macromolecules* **1986**, *19*, 2020.
- (32) Kramer, E. J.; Berger, L. L. *AdV. Polym. Sci.* **1990**, *91/92*, 1.
- (33) Yang, A. C. M.; Kunz, M. S.; Logan, J. A. *Macromolecules* **1993**, *26*, 1776.
- (34) Lin, J. H.; Yang, A. C. M. *Macromolecules* **2001**, *34*, 3698.
- (35) Lin, C. H.; Yang, A. C. M. *Macromolecules* **2001**, *34*, 4865.
- (36) Yang, A. C. M.; Wang, R. C.; Lin, J. H. *Polymer* **1996**, *37*, 5751.
- (37) Yang, A. C.-M.; Wang, R. C.; Kunz, M. S.; Yang, I. C. *J. Polym. Sci.: Polym. Phys. Ed.* **1996**, *34*, 1141.
- (38) Hsiao, C. C.; Lin, T. S.; Cheng, L. Y.; Ma, C. C. M.; Yang, A. C. M. *Macromolecules* **2005**, *38*, 4811.
- (39) Lin, T. S.; Cheng, L. Y.; Hsiao, C. C.; Yang, A. C. M. *Mater. Chem. Phys.* **2005**, *94*, 438.
- (40) Kong, H.; Gao, C.; Yan, D. *Macromolecules* **2004**, *37*, 4022.
- (41) Bridgman, D. W. *Studies in Large Plastic Flow and Fracture*; Harvard University Press: Cambridge, U.K., 1964: p 9.
- (42) Hutchinson, J. W.; Neale, K. W. *J. Mech. Phys. Solids* **1983**, *31*, 405.
- (43) G'sell, C.; Marquez-Lucero, A. *Polymer* **1993**, *34*, 2740.
- (44) Rubinstein, M.; Colby, R. H. *Polymer Physics*, Oxford University Press, Oxford, 2003; Chapter 9.
- (45) The area of the confining tube (A_{chain}) for a single PS chain was calculated by A_{chain} = $M_0 / (N_{Av} F b)$ where M_0 is the molar mass of a Kuhn monomer, N_{Av} is Avogadro's number, F is the density, and b is the Kuhn length.
- (46) A polymer segment in the wormlike tube has to move a contour length of $l = bN$ to produce a translational distance of $R = bN^{1/2}$. Therefore, the sliding velocity within the

tube is $N^{1/2}$ times the linear velocity measured from deformation zone widening.

(47) Cotiuga, I.; Picchioni, F.; Agarwal, U. S.; Wouters, D.; Loos, J.; Lemstra, P. *Macromol. Rapid Commun.* **2006**, *27*, 1073.

(48) Doi, M.; Edwards, S. F. *The Theory of Polymer Dynamics*; Clarendon: Oxford, U.K., 1986; p 338.

(49) Yang, A. C.-M. Micro-mechanisms of deformation, conduction percolation and nanotube crosslinking via surface grafting polymerization in CNT-polymer nanocomposites. The 4th US Air Force-Taiwan Nanoscience Initiative Workshop, University of Houston, Houston, TX, February 8-9, 2007.

(50) Lee, J. Y.; Zhang, Q.; Emrick, T.; Crosby, A. J. *Macromolecules* **2006**, *39*, 7392.